nature cancer

ARTICLES

https://doi.org/10.1038/s43018-020-00160-x

Check for updates

Targeting glutamine dependence through *GLS1* inhibition suppresses *ARID1A*-inactivated clear cell ovarian carcinoma

Shuai Wu[1], Takeshi Fukumoto[1], Jianhuang Lin[1], Timothy Nacarelli[1], Yemin Wang[2,3], Dionzie Ong[2], Heng Liu[1], Nail Fatkhutdinov[1], Joseph A. Zundell[1], Sergey Karakashev[1], Wei Zhou[1], Lauren E. Schwartz[4], Hsin-Yao Tang[5], Ronny Drapkin[6], Qin Liu[7], David G. Huntsman[2], Andrew V. Kossenkov[1], David W. Speicher[5,7], Zachary T. Schug[7], Chi Van Dang[7,8] and Rugang Zhang[1]✉

Alterations in components of the SWI/SNF chromatin-remodeling complex occur in ~20% of all human cancers. For example, *ARID1A* is mutated in up to 62% of ovarian clear cell carcinomas (OCCC), a disease lacking effective therapies. Here we show that *ARID1A* mutation creates a dependence on glutamine metabolism. SWI/SNF represses glutaminase (*GLS1*) and *ARID1A* inactivation upregulates *GLS1*. *ARID1A* inactivation increases glutamine utilization and metabolism through the tricarboxylic acid cycle to support aspartate synthesis. Indeed, glutaminase inhibitor CB-839 suppresses the growth of *ARID1A* mutant, but not wild-type, OCCCs in both orthotopic and patient-derived xenografts. In addition, glutaminase inhibitor CB-839 synergizes with immune checkpoint blockade anti-PD-L1 antibody in a genetic OCCC mouse model driven by conditional *Arid1a* inactivation. Our data indicate that pharmacological inhibition of glutaminase alone or in combination with immune checkpoint blockade represents an effective therapeutic strategy for cancers involving alterations in the SWI/SNF complex, such as *ARID1A* mutations.

The SWI/SNF chromatin-remodeling complex remodels nucleosomes to modulate transcription[1]. *ARID1A* functions as a repressor or activator of gene transcription through localizing to promoters or enhancers[2,3]. The SWI/SNF complex is genetically altered in ~20% of human cancers[1,4]. *ARID1A* is among the most frequently mutated genes across human cancers[1,4,5]. For example, *ARID1A* is mutated in up to 62% of OCCC[6–8]. Over 90% of *ARID1A* mutations in OCCC lead to loss of protein expression[6–8]. OCCC is generally refractory to the standard-of-care chemotherapy and when diagnosed at advanced stages, carries the worst prognosis among all histosubtypes of ovarian cancer[9]. Therefore, there is an urgent need for effective therapeutic approaches for this devastating disease. There is evidence to suggest that metabolic reprogramming is implicated in OCCC[10]. However, clinically applicable therapeutic approaches targeting metabolism in OCCC remain to be explored.

Glutamine, a non-essential amino acid, contributes to biosynthetic pathways in proliferating cells[11]. Glutaminase (GLS) is an amidohydrolase that generates glutamate from glutamine[12]. GLS is encoded by two genes in humans, *GLS1* and *GLS2* (ref. [12]). *GLS1* is broadly expressed, whereas *GLS2* is primarily expressed in the liver[13,14]. However, the role of the *ARID1A*-containing SWI/SNF complex in regulating glutamine metabolism remains to be fully explored.

While there are reports that SWI/SNF complex inactivation renders tumors sensitive to immune checkpoint inhibition[15–19], others did not find a consistent association between SWI/SNF genomic alterations and improved clinical outcome to immune checkpoint inhibitors[20]. Notably, *ARID1A* mutation sensitizes ovarian cancer to immune checkpoint blockades such as anti-PD-L1 (refs. [19,21]). Indeed, there was a trend toward improved response rate toward immune checkpoint blockade in OCCC in clinical trials[22]. However, anti-PD-L1 treatment only has a modest effect on improving survival of mice bearing ARID1A-inactivated tumors[19,21]. This suggests that to achieve complete eradication of *ARID1A*-mutated ovarian cancer, combination therapeutic strategies are necessary.

Here we show that *ARID1A* mutation creates a dependence on glutamine metabolism and clinically applicable glutamine inhibitor CB-839 alone or in combination with immune checkpoint blockade represents an effective therapeutic strategy for cancers involving alterations in the SWI/SNF complex, such as *ARID1A* mutations.

Results

ARID1A inactivation creates a dependence on glutamine. To explore the potential role of ARID1A in regulating metabolic reprogramming, we knocked out *ARID1A* in *ARID1A* wild-type RMG1 OCCC cells to mimic loss of ARID1A protein expression caused by >90% of *ARID1A* mutations (Extended Data Fig. 1a). Notably, *ARID1A* knockout does not affect cell growth rates[23]. We compared steady-state metabolic profiles by liquid chromatography-tandem mass spectrometry (LC–MS/MS) in *ARID1A* wild-type and *ARID1A* knockout RMG1 OCCC cells. Compared with *ARID1A*

[1]Immunology, Microenvironment & Metastasis Program, The Wistar Institute, Philadelphia, PA, USA. [2]Department of Pathology and Laboratory Medicine, University of British Columbia, Vancouver, British Columbia, Canada. [3]Department of Molecular Oncology, British Columbia Cancer Research Centre, Vancouver, British Columbia, Canada. [4]Department of Pathology and Laboratory Medicine, University of Pennsylvania, Philadelphia, PA, USA. [5]Proteomics and Metabolomics Facility, The Wistar Institute, Philadelphia, PA, USA. [6]Department of Obstetrics and Gynecology, Penn Ovarian Cancer Research Center, University of Pennsylvania, Philadelphia, PA, USA. [7]Molecular and Cellular Oncogenesis Program, The Wistar Institute, Philadelphia, PA, USA. [8]Ludwig Institute for Cancer Research, New York, NY, USA. ✉e-mail: rzhang@wistar.org

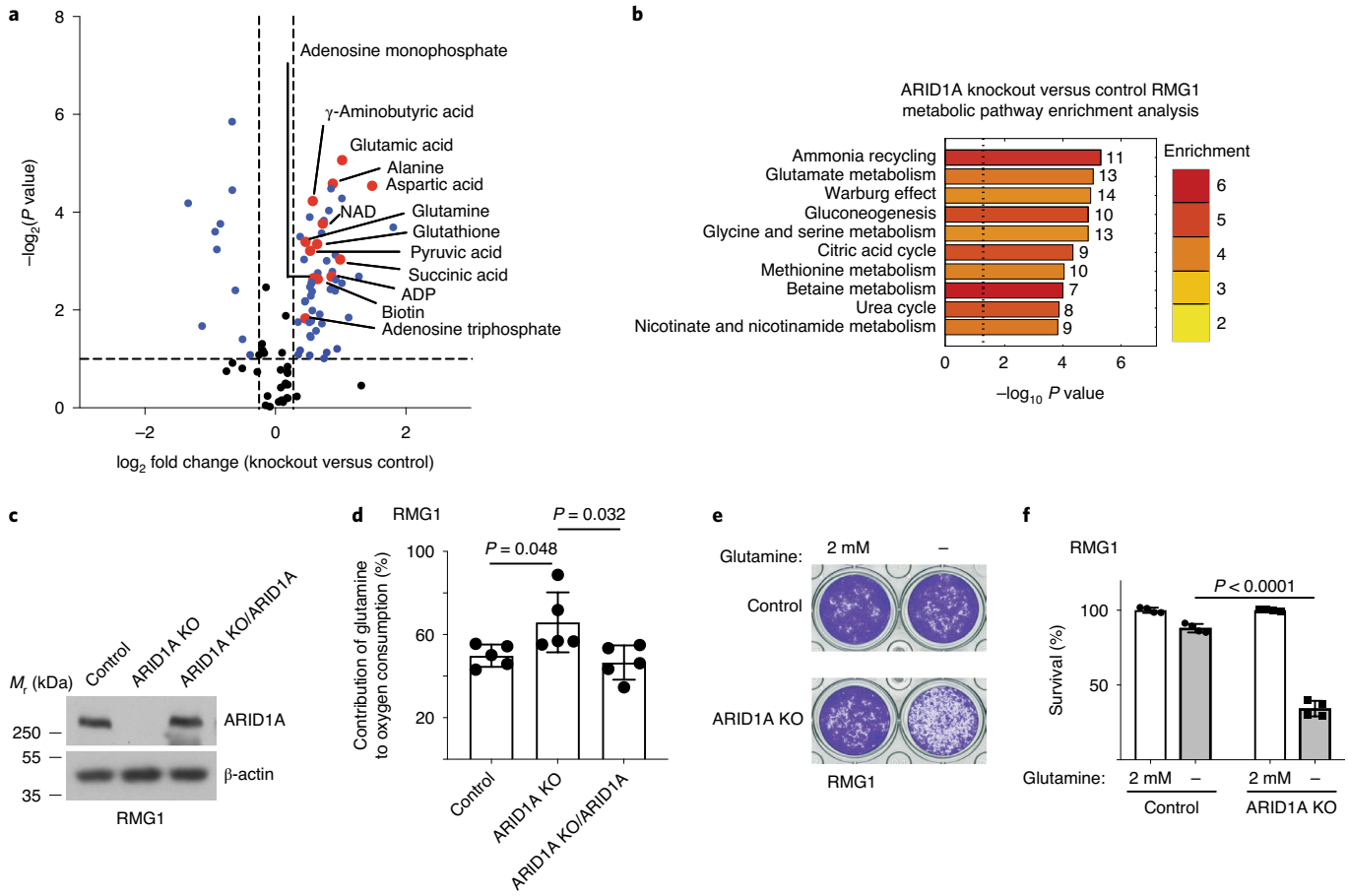

Fig. 1 | ARID1A inactivation creates a dependence on glutamine. a, Volcano plot showing changes for metabolites between control and *ARID1A* knockout RMG1 cells. Blue indicates changes used for enrichment analysis and red labels metabolites in glutamine metabolism. Plot shows average of three independent experiments (included separately as source data). **b**, Top ten metabolic pathways enriched by *ARID1A* knockout in RMG1 cells determined by metabolites set enrichment analysis (MSEA). **c**, ARID1A expression in parental, *ARID1A* knockout RMG1 cells with or without wild-type ARID1A restoration determined by immunoblot. Shown are representatives of three independent experiments with similar results. **d**, Contribution of glutamine to oxygen consumption in the indicated cells analyzed by Seahorse, $n = 5$ independent experiments. **e**,**f**, Colony formation (**e**) and quantification (**f**) of parental and *ARID1A* knockout RMG1 cells cultured in medium with or without glutamine deprivation for 12 d. Shown are representative of four independent experiments with similar results in **e**, $n = 4$ independent experiments in **f**. Error bars represent mean with s.d. in **d** and **f**. *P* values were calculated using two-tailed Student's *t*-test in **a**, **d**, **f** and Fisher's least significant difference test in **b**.

wild-type controls, the glutamate metabolism/ammonia recycling pathway was significantly enriched by *ARID1A* knockout in RMG1 cells (Fig. 1a,b and Supplementary Table 1). Consistently, contribution of glutamine to oxygen consumption was significantly increased by *ARID1A* knockout as determined by Seahorse analysis, which was rescued by restoration of ARID1A expression in these cells (Fig. 1c,d). Indeed, compared with *ARID1A* wild-type cells, *ARID1A* knockout cells significantly exacerbated the growth suppression induced by glutamine deprivation (Fig. 1e,f). Similar observations were made in additional isogenic *ARID1A* wild-type and knockout OCCC cell lines (Extended Data Fig. 1b–e). Notably, glucose uptake was decreased by *ARID1A* knockout (Extended Data Fig. 1f,g), which correlates with a decrease in sensitivity to glucose deprivation (Extended Data Fig. 1h). These results indicate that ARID1A inactivation creates a dependence on glutamine.

Inactivation of SWI/SNF complex increases *GLS1* expression. We next sought to determine the mechanism underlying the observed glutamine dependence by ARID1A inactivation. Toward this goal, we cross-referenced ARID1A chromatin immunoprecipitation followed by next generation sequencing (ChIP-seq) analysis in *ARID1A* wild-type RMG1 cells with differentially expressed genes based on RNA-seq analysis in *ARID1A* wild-type control and knockout RMG1 cells. The analysis revealed *GLS1* as the top direct ARID1A target gene that was significantly upregulated by *ARID1A* knockout in the glutamine metabolic pathway (Fig. 2a and Extended Data Fig. 2a), suggesting that ARID1A functions as a transcriptional repressor of *GLS1*. Consistently, *GLS1* is also a target of SNF5, a core subunit of the SWI/SNF complex and *ARID1A* knockout increased the association of RNA polymerase II (Pol II) with the *GLS1* promoter in RMG1 cells (Extended Data Fig. 2b). Similarly, data mining of published ChIP-seqs showed that *GLS1* is a direct target of SWI/SNF subunits, such as ARID1A, SNF5, SMARCA4 and BAF155 (Extended Data Fig. 2c). This correlates with a general increase in accessibility of the *GLS1* promoter determined by assay for transposase-accessible chromatin using sequencing (ATAC-seq) (Extended Data Fig. 2d). However, although there is a trend toward an increase in accessibility of the *GLS1* promoter in the HCT116 cell line, the increase is less robust compared with other cell lines (Extended Data Fig. 2d).

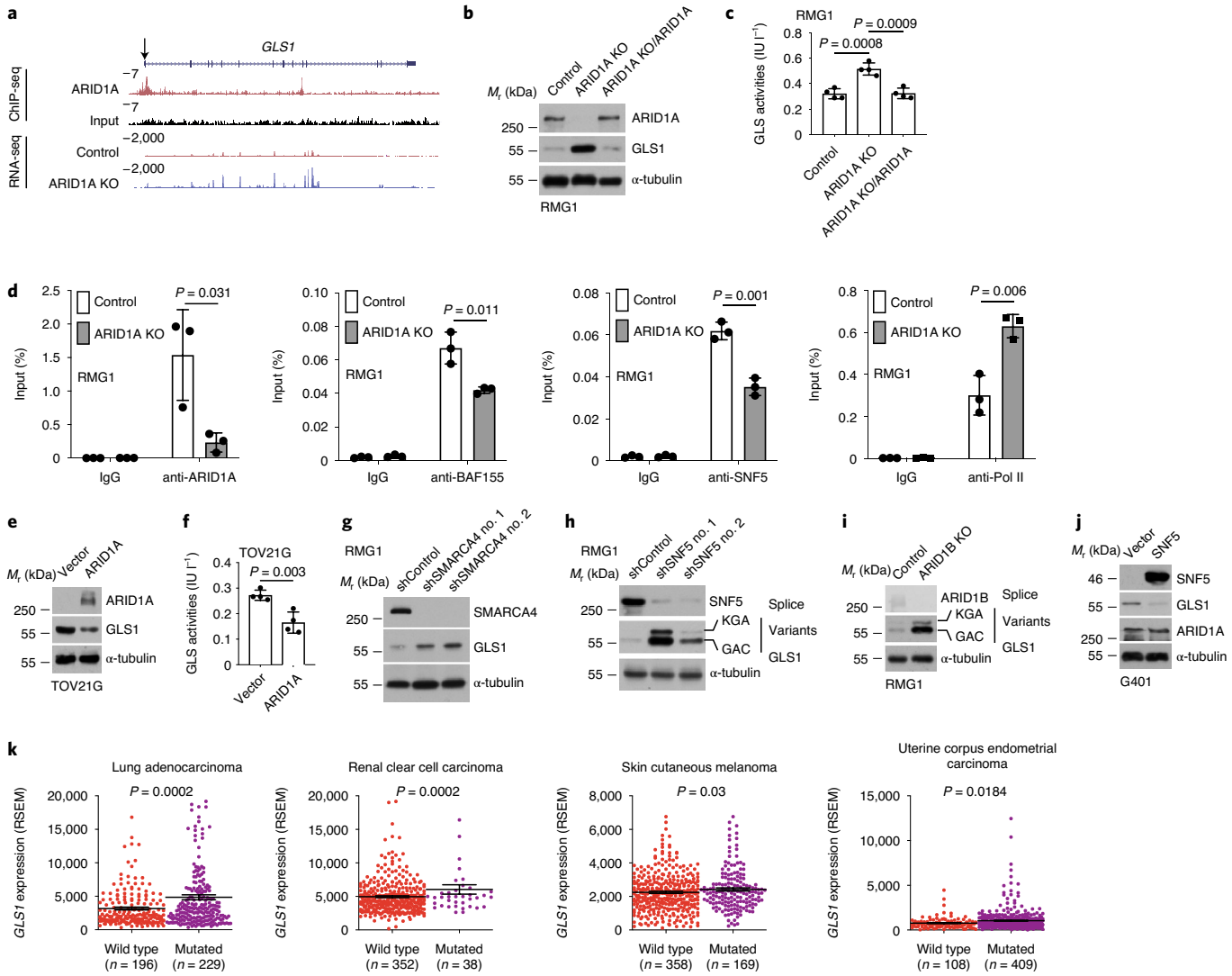

Fig. 2 | *GLS1* is a direct target of the SWI/SNF complex. a, ARID1A ChIP-seq and input tracks and RNA-seq tracks in the *GLS1* gene locus in parental and *ARID1A* knockout RMG1 cells. Shown are representatives of three independent experiments with similar results. **b**,**c**, Parental and *ARID1A* knockout RMG1 cells with or without wild-type *ARID1A* restoration were examined for expression of ARID1A and GLS1 by immunoblot (**b**) or measured for GLS activity (**c**), $n = 4$ independent experiments. **d**, The association of ARID1A, BAF155, SNF5 and RNA Pol II with the *GLS1* gene promoter in the indicated cells was examined by ChIP–qPCR analysis. An isotype-matched IgG was used as a negative control, $n = 3$ independent experiments. **e**,**f**, *ARID1A*-mutated TOV21G cells with or without wild-type ARID1A restoration were examined for ARID1A and GLS1 expression by immunoblot (**e**) or measured for GLS activity (**f**), $n = 4$ independent experiments. **g**–**i**, RMG1 cells with *SMARCA4* knockdown (**g**), *SNF5* knockdown (**h**) or *ARID1B* knockout (**i**) were examined for GLS1 expression by immunoblot. **j**, *SNF5* mutant G401 cells with or without wild-type *SNF5* restoration were examined for SNF5, GLS1 and ARID1A expression by immunoblot. **k**, GLS1 is expressed at a significantly higher levels in cancers with mutations in subunits of the SWI/SNF complex in the indicated cancer types in the TCGA dataset. Immunoblots are representative of two independent experiments with similar results in **b**, **e**, **g**–**j**. Error bars represent mean with s.d. in **c**, **d**, **f** and **k**. *P* values were calculated using two-tailed Student's *t*-test in **c**, **d**, **f** and **k**.

Likewise, upregulation of *GLS1* by *ARID1A* knockout was also observed in the published RNA-seq databases (Extended Data Fig. 2e). We validated upregulation of *GLS1* expression and increase in GLS activity in *ARID1A* knockout RMG1 cells (Fig. 2b,c). Notably, the observed increase in both *GLS1* expression and GLS activity was rescued by restoration of ARID1A expression, indicating these are ARID1A expression-dependent instead of potential off-target effects (Fig. 2b,c). In addition, ARID1A and other core subunits of the SWI/SNF complex, such as BAF155 and SNF5, directly bound to the *GLS1* promoter as determined by cut-run or ChIP–qPCR analysis (Fig. 2d). Notably, the association of BAF155 and SNF5 with the *GLS1* promoter was reduced by *ARID1A* knockout (Fig. 2d), suggesting that the observed repression of *GLS1* by ARID1A is SWI/SNF complex-dependent. The enhanced association of RNA Pol II with the *GLS1* promoter by *ARID1A* knockout was also validated (Fig. 2d). Similar findings were made in additional *ARID1A* wild-type and knockdown or knockout isogenic cell lines (Extended Data Fig. 2f–i). Conversely, restoration of wild-type *ARID1A* expression in *ARID1A*-mutated cells suppressed *GLS1* expression and reduced GLS activity (Fig. 2e,f and Extended Data Fig. 2j). Because mutations in *ARID1A* and *TP53* are typically mutually exclusive[24,25] and p53 is extensively implicated in metabolic regulation[26], we focused our analysis on cancer cell lines with

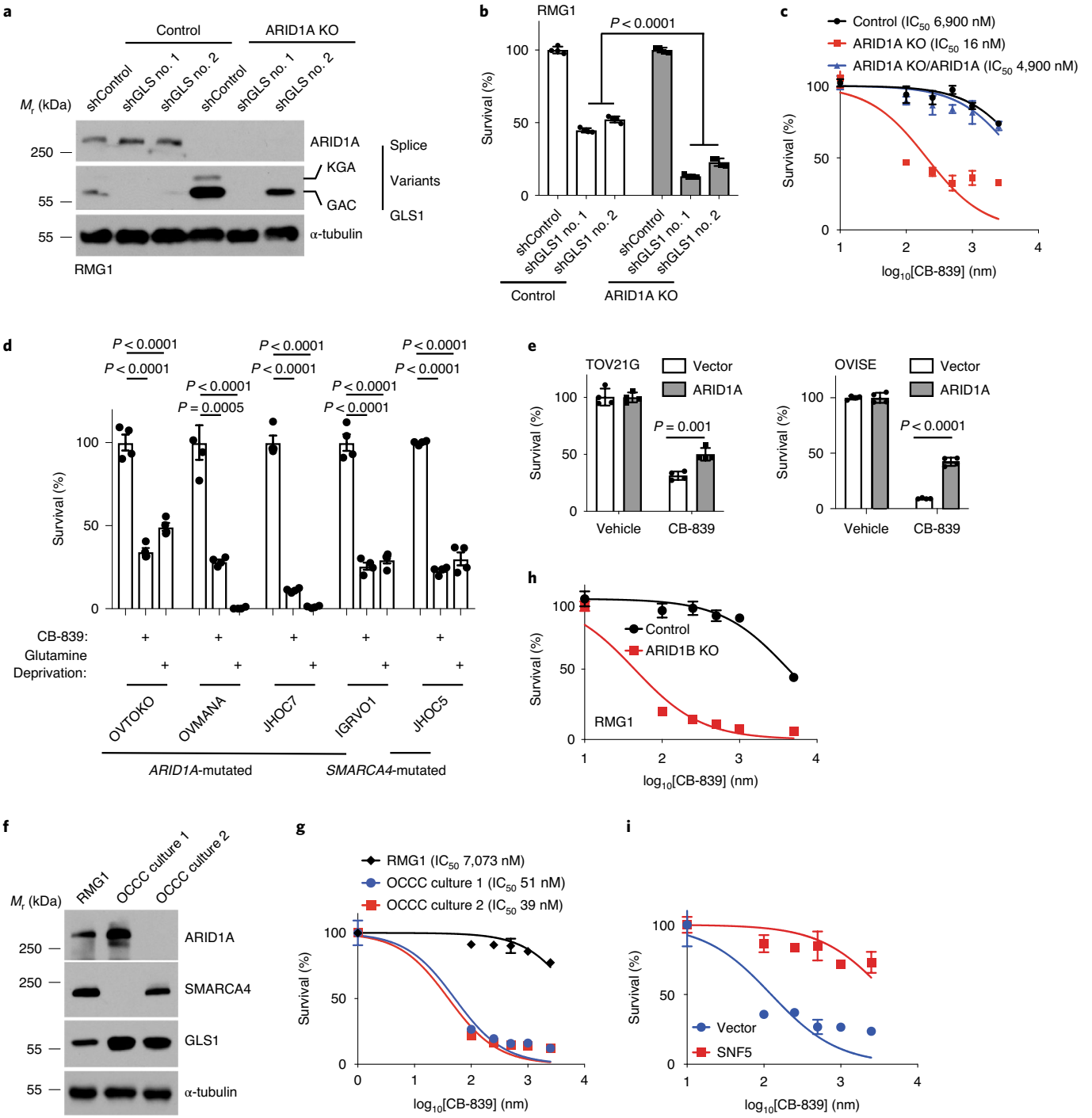

Fig. 3 | Inactivation of the SWI/SNF complex sensitizes cells to GLS inhibition. a,**b**, Parental and *ARID1A* knockout RMG1 cells expressing the indicated shGLS1s or control were examined for ARID1A and GLS1 expression by immunoblot (**a**) or subjected to colony formation and the colonies formed by the indicated cells were quantified (**b**), $n = 4$ independent experiments. **c**, Dose–response curves of indicated parental and *ARID1A* knockout RMG1 cells with or without wild-type ARID1A restoration to GLS inhibitor CB-839 determined by colony-formation assay, $n = 4$ independent experiments. **d**, Growth inhibition of indicated *ARID1A* or *SMARCA4*-mutated OCCC cell lines treated with 0.5 μM CB-839 or glutamine deprivation based on a 12-d colony-formation assay, $n = 4$ independent experiments. **e**, Quantification of growth of TOV21G and OVISE cells with or without wild-type ARID1A restoration treated with or without 0.05 μM or 10 μM CB-839 for 12 d based on colony-formation assay, $n = 4$ independent experiments. **f**, Expression of ARID1A and GLS1 in the indicated ARID1A or SMARCA4-inactivated primary OCCC cultures. **g**, Dose–response curves of indicated ARID1A or SMARCA4-inactivated primary OCCC cultures to GLS inhibitor CB-839 determined by colony-formation assay. RMG1 cells were used as a control, $n = 4$ independent experiments. **h**, Dose–response curves of indicated parental and ARID1B knockout RMG1 cells to GLS inhibitor CB-839 determined by colony-formation assay, $n = 4$ independent experiments. **i**, Dose–response curves of indicated parental and wild-type SNF5 restored G401 cells to GLS inhibitor CB-839 determined by colony-formation assay, $n = 4$ independent experiments. Immunoblots are representative of two independent experiments with similar results in **a** and **f**. Error bars represent mean with s.d. in **b**–**e**, **g**–**i**. *P* values were calculated using Student's two-tailed *t*-test in **b**, **d** and **e**.

wild-type *TP53*. Indeed, *GLS1* expression negatively correlates with *ARID1A* expression in *TP53* wild-type cancer cell lines across cancer types according to the Cancer Cell Line Encyclopedia RNA-seq database (Extended Data Fig. 2k)[27].

As repression of GLS1 by ARID1A correlates with changes in the SWI/SNF complex in the *GLS1* promoter, we examined whether inactivation of other SWI/SNF components will have similar effects on GLS1 expression. Indeed, knockdown of *ARID1B*, *SMARCA4* (also known as BRG1) or *SNF5* subunits of the SWI/SNF complex also upregulated *GLS1* expression (Fig. 2g–i). Conversely, restoration of SNF5 expression in *SNF5*-mutated rhabdoid tumor cells downregulated *GLS1* expression (Fig. 2j). Since OCCC was not included in The Cancer Genome Atlas (TCGA) database, we explored the correlation between *GLS1* expression and mutations in the SWI/SNF complex in lung adenocarcinoma, renal clear cell carcinoma, skin cutaneous melanoma and uterine corpus endometrial carcinoma, in which a high frequency of mutations in the SWI/SNF subunits are observed[4]. Indeed, GLS1 is expressed at a significantly higher levels in *TP53* wild-type tumors with mutations in the SWI/SNF complex (Fig. 2k). Together, we conclude that SWI/SNF complex functions as a repressor of GLS1 expression.

ARID1A inactivation sensitizes cells to GLS inhibition. As ARID1A inactivation creates glutamine dependence and upregulates *GLS1* expression, we next sought to determine whether ARID1A inactivation sensitizes cells to GLS1 inhibition. Toward this goal, we inhibited GLS1 activity both genetically by short hairpin (shRNA)-mediated knockdown and using a small molecule inhibitor of GLS activity. Indeed, genetically knocking down GLS1 expression was significantly more effective in suppressing the growth of *ARID1A* knockout cells compared to controls (Fig. 3a,b and Extended Data Fig. 3a). We also tested CB-839, a specific GLS inhibitor[28], in *ARID1A* wild-type control and knockout RMG1 cells. We chose CB-839 for our experiments because it is the only GLS inhibitor that is now in clinical trials for other diseases and is proven safe in clinical trials, including in combination studies[28,29]. Indeed, compared with *ARID1A* wild-type control cells, *ARID1A* knockout significantly decreased the half-maximum inhibitory concentration (IC_{50}) of CB-839 in RMG1 cells by >300-fold (Fig. 3c). The observed effects are ARID1A-dependent because the decrease in CB-839 IC_{50} can be rescued by ectopic expression of wild-type *ARID1A* (Fig. 3c). In addition, similar growth inhibition was observed in additional *ARID1A* or *SMARCA4*-mutated OCCC cell lines treated with CB-839 or glutamine deprivation (Fig. 3d and Extended Data Fig. 3b). Notably, restoration of ARID1A expression in *ARID1A*-mutated cells significantly reduced the sensitivity to CB-839 (Fig. 3e). Likewise, CB-839 was effective in suppressing the growth of ARID1A or SMARCA4-inactivated primary OCCC cultures (Fig. 3f,g). Notably, the IC_{50} of CB-839 was comparable between ARID1A or SMARCA4-inactivated primary OCCC cultures compared with *ARID1A* knockout cells (Fig. 3c,g). In addition, the IC_{50} of CB-839 was comparable between *ARID1A*-mutated TOV21G OCCC cells and *VHL*-deficient renal clear cell carcinoma cell lines that are hypersensitive to CB-839 (Extended Data Fig. 3c)[30]. Consistent with the observed upregulation of GLS1 by *ARID1A* knockout, *ARID1B* knockout sensitized RMG1 cells to CB-839 (Fig. 3h). Further supporting the notion that the observed effects are SWI/SNF-dependent, restoration of SNF5 expression in *SNF5*-mutated rhabdoid tumor cells significantly increased the IC_{50} of CB-839 (Fig. 3i). Indeed, in the Project Achilles synthetic lethality database, *GLS1* shRNA was more effective in suppressing the growth of cell lines with mutations in subunits of the SWI/SNF complex compared with wild-type cell lines (Extended Data Fig. 3d)[31]. For example, for skin cancer cell lines in the database, *GLS1* shRNA was significantly more effective against SWI/SNF mutant compared with wild-type cell lines (Extended Data Fig. 3e)[31]. Together, we conclude that inactivation of the SWI/SNF complex sensitizes cells to GLS1 inhibition. Notably, ectopic GLS1 expression did not affect sensitivity to CB-839 in *ARID1A* wild-type RMG1 cells (Extended Data Fig. 3f,g). This is consistent with previous reports that GLS1 upregulation alone is not sufficient to confer sensitivity to CB-839 (refs. [32,33]).

ARID1A inactivation increases glutamine utilization and metabolism through the tricarboxylic acid cycle to support aspartate and nucleotide synthesis. We next sought to determine how ARID1A status differentially affects glutamine utilization. Toward this goal, we performed LC–MS/MS-based analysis of metabolites in *ARID1A* wild-type control and knockout RMG1 OCCC cells with or without GLS inhibition by CB-839. Metabolic profiling revealed that ARID1A inactivation increases glutamine utilization by the tricarboxylic acid (TCA) cycle and the use of glutamine to support aspartate and nucleotide biosynthesis (Fig. 4a). Pathway analysis revealed the malate–aspartate shuttle as the top pathway enriched based on the differential response to CB-839 between *ARID1A* knockout cells and controls (Fig. 4b). This further supports that ARID1A inactivation promotes aspartate and nucleotide synthesis from glutamine through the TCA cycle. Cells were next incubated with $^{13}C_5$-glutamine to infer glutamine metabolism and associated metabolic pathways. The $^{13}C_5$-glutamine stable isotope tracer analysis revealed that *ARID1A* knockout increased the metabolism through glutamate, TCA cycle metabolites (such as α-ketoglutarate and citrate), aspartate and nucleotides (such as UMP) (Fig. 4c,d). This suggests that in addition to increasing glutamine uptake by upregulating *GLS1*, *ARID1A* inactivation also increased the utilization of key glutamine metabolism metabolites such as aspartate to support the growth of ARID1A-inactivated cells. Consistently, aspartate utilization was increased by *ARID1A* knockout as indicated by the increase in metabolites such as AMP, UMP and *N*-acetylaspartate (Extended Data Fig. 4a). Consistent with these findings, addition of aspartate in the culture medium of *ARID1A*-mutated or knockout cells reduced sensitivity to CB-839 (Fig. 4e and Extended Data Fig. 4b). In addition, ectopic expression of aspartate transporter *SLC1A3* in RMG1 knockout cells that do not express endogenous *SLC1A3*, reduced sensitivity to CB-839 (Fig. 4f and Extended Data Fig. 4c,d), further supporting that the observed effects are due to changes in aspartate. Finally, supporting

Fig. 4 | *ARID1A* inactivation increases glutamine-dependent aspartate biosynthesis. a, Control and *ARDI1A* knockout RMG1 cells treated with or without GLS inhibitor CB-839 were subjected to LC–MS/MS analysis. Heat map indicates fold changes in comparison to parental control without CB-839 treatment, $n = 3$ independent experiments. WT, wild type; AKO, *ARID1A* knockout; CB, CB-839; OXPHOS, oxidative phosphorylation. **b**, Analysis of metabolic pathways enriched in CB-839 treated *ARID1A* knockout RMG1 cells compared with CB-839-treated parental RMG1 cells. **c**, Schematic of glutamine tracing of aspartate biogenesis. **d**, Indicated cells were incubated for 16 h in the presence of $^{13}C_5$-glutamine and intracellular metabolites were extracted for analysis by LC–MS to evaluate glutamine-dependent metabolism. Mass isotopologs ($M+X$) analysis of the indicated metabolites are shown as percentage of indicated number of carbons labeled with heavy isotype, $n = 3$ independent experiments. **e**, Quantification of colony formation of TOV21G cells treated with or without 0.05 μM CB-839 cultured in medium supplemented with or without 5 mM aspartate, $n = 4$ independent experiments. **f**, Quantification of colony formation by *ARID1A* knockout RMG1 cells with or without ectopic aspartate transport SLC1A3 expression cultured in medium supplemented with 5 mM aspartate treated with or without the indicated concentration of CB-839, $n = 4$ independent experiments. KO, knockout. Error bars represent mean with s.d. in **d**–**f**. *P* values were calculated using two-tailed Student's *t*-test in **a**, **d**–**f** and Fisher's least significant difference test in **b**.

the notion that the increase in aspartate generated from glutamine in *ARID1A*-inactivated cells was utilized for nucleotide synthesis, CB-839 treatment significantly reduced S phase of the cell cycle, where nucleotide is utilized for DNA replication (Extended Data Fig. 4e). Consistent with RNA-seq results and further highlighting the role of *ARID1A*-regulated *GLS1* in observed changes in gluta-

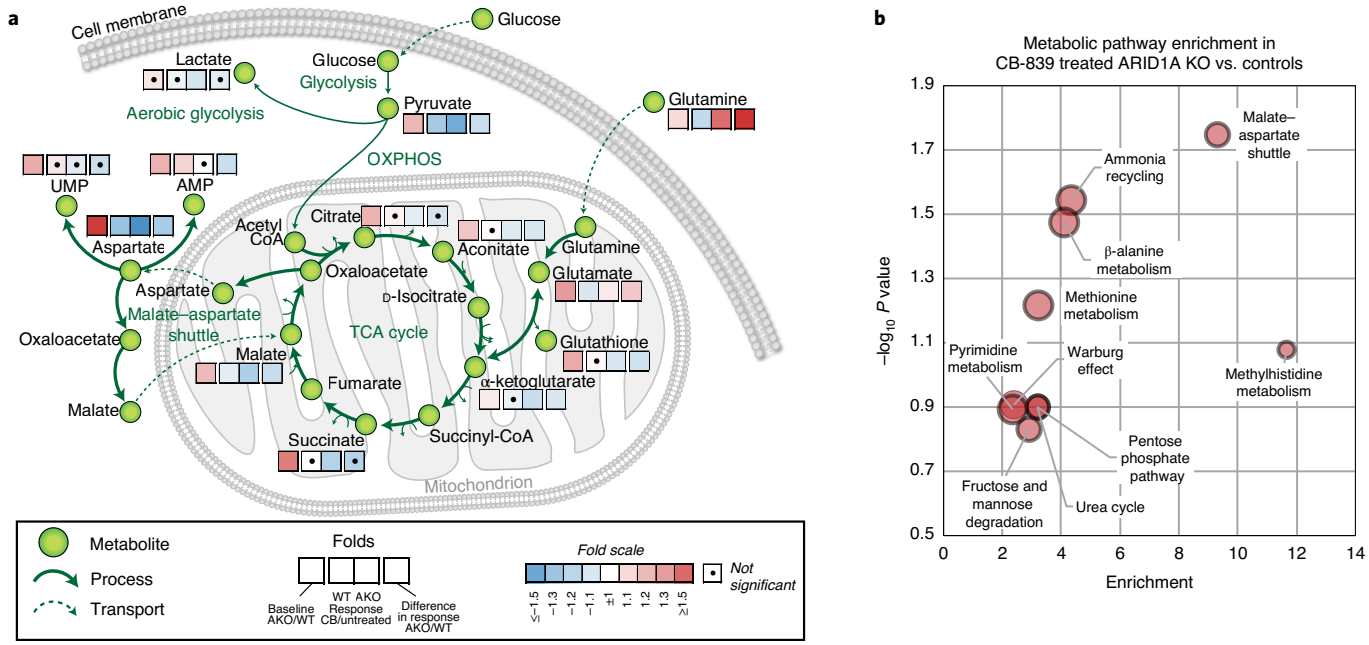

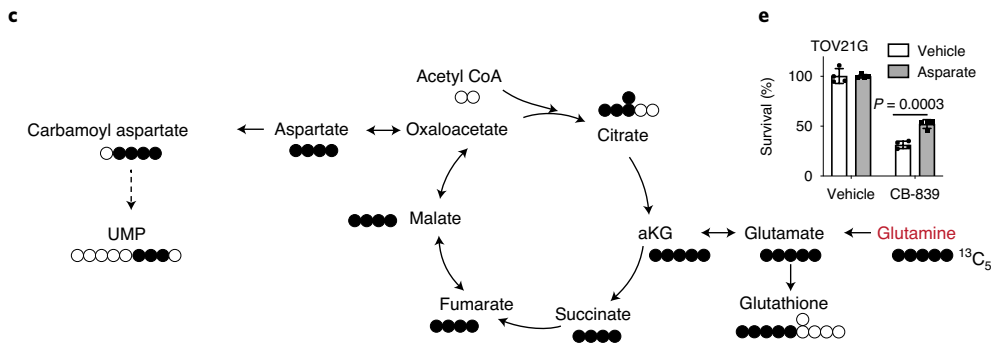

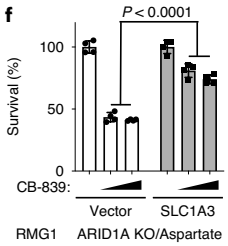

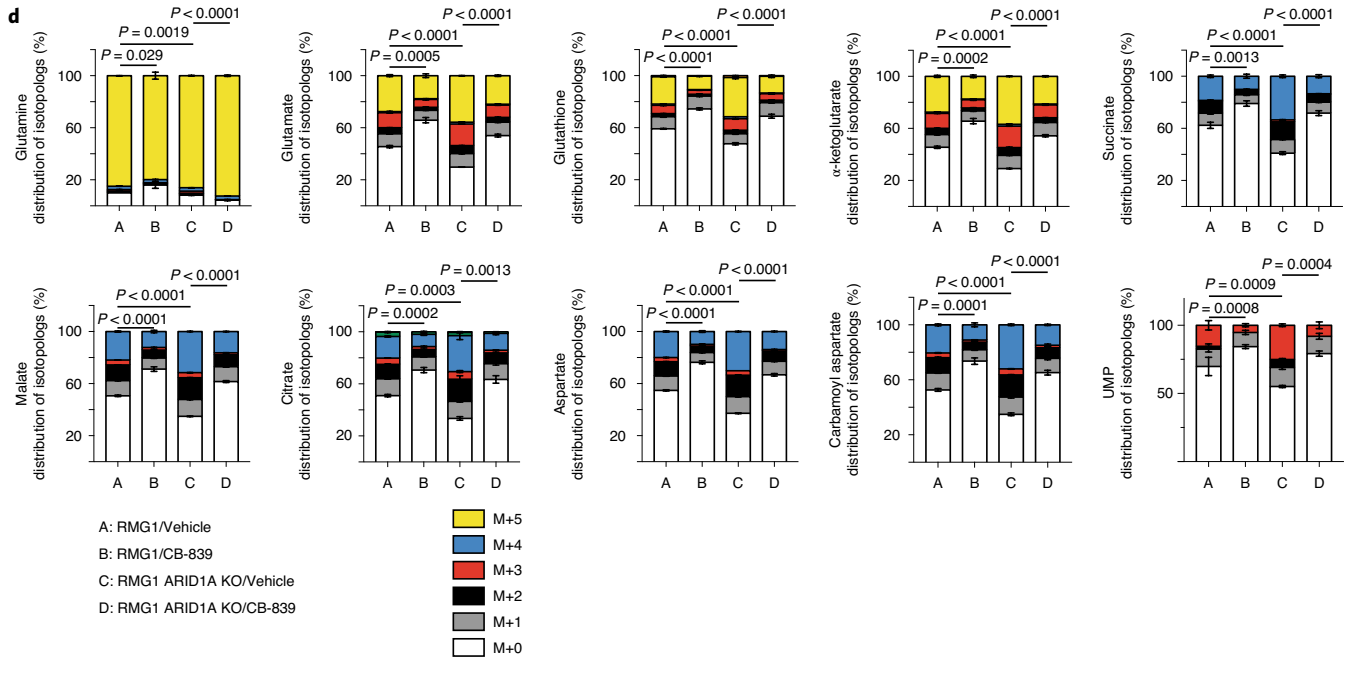

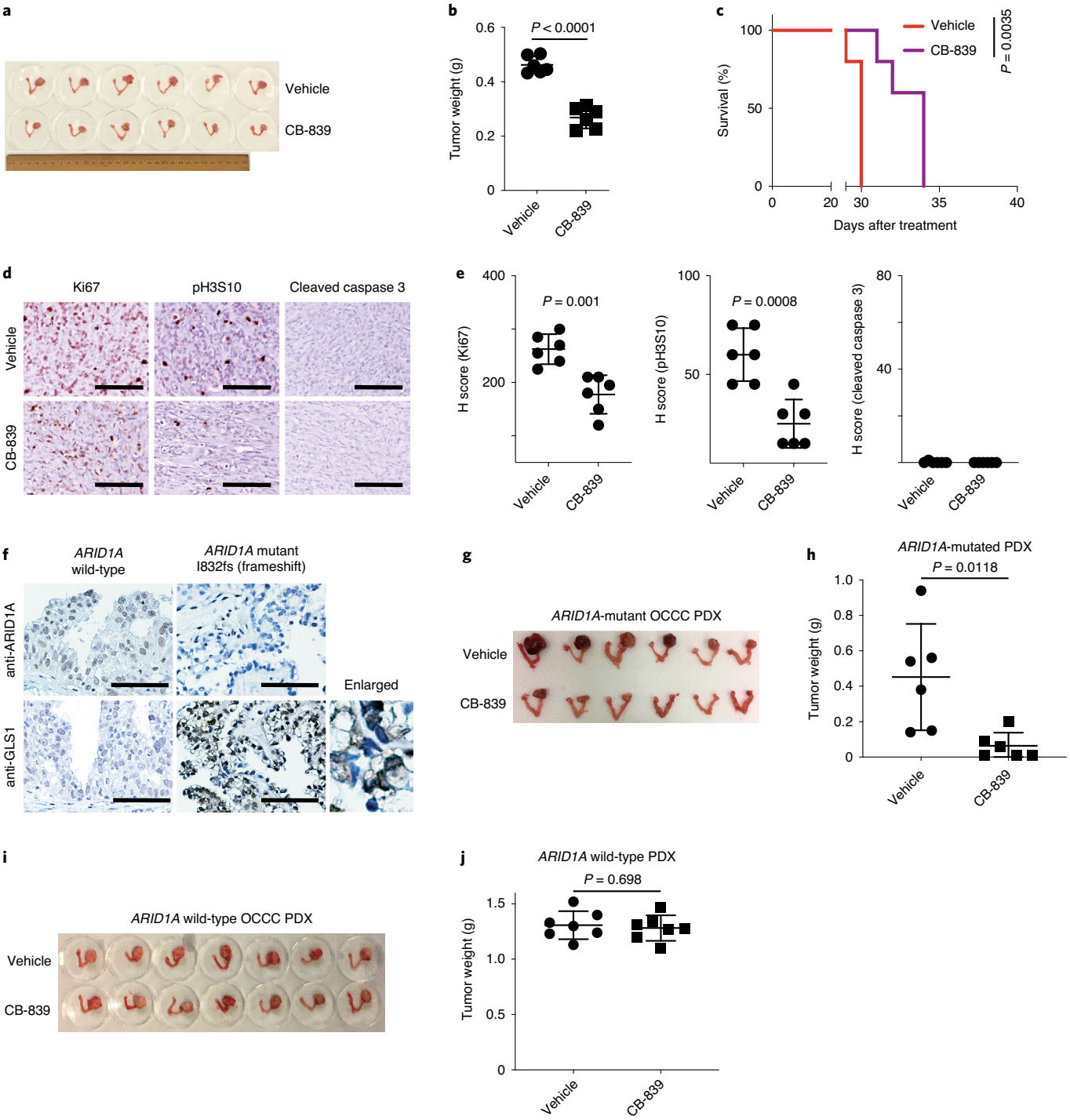

Fig. 5 | GLS inhibition suppresses growth of ARID1A-inactivated OCCCs in vivo. a–**e**, Orthotopic xenografts formed by *ARID1A*-mutated TOV21G cells were treated with vehicle or CB-839. Shown are images of reproductive tracks with tumors from indicated groups at the end of treatment (**a**). Tumor weight was measured as a surrogate for tumor burden ($n = 6$ mice per group) (**b**). After stopping the treatment, mice from indicated treatment groups were followed for survival by the Kaplan–Meier method ($n = 5$ mice per group) (**c**). Dissected tumors from indicated treatment groups were subjected to immunohistochemical (IHC) staining for cell proliferation marker Ki67, mitotic marker pH3S10 or apoptosis marker cleaved caspase 3 on serial sections (**d**) and the histological score (H-score) of indicated markers was quantified from three separate fields from six tumors from six individual mice in each of the indicated treatment groups (**e**). Scale bar, 100 μm. **f**, Expression of ARID1A and GLS1 in indicated *ARID1A* wild-type or mutated OCCC PDXs determined by IHC staining. Shown are representative images of three independent technical replicates from the same pair of *ARID1A* wild-type and mutant PDXs. Scale bars, 100 μm. **g**,**h**, Mice bearing *ARID1A*-mutated OCCC PDXs were treated with vehicle or CB-839 ($n = 6$ mice per group). Shown are images of reproductive tracks with tumors from indicated groups at end of treatment (**g**). Tumor weight was measured as surrogate for tumor burden (**h**). **i**,**j**, Same as **g**,**h**, but for *ARID1A* wild-type OCCC PDXs ($n = 7$ mice per group). Error bars represent mean with s.d. in **b**, **e**, **h** and **j**. *P* values were calculated using two-tailed Student's *t*-test in **b**, **e**, **h**, **j** and log-rank test in **c**.

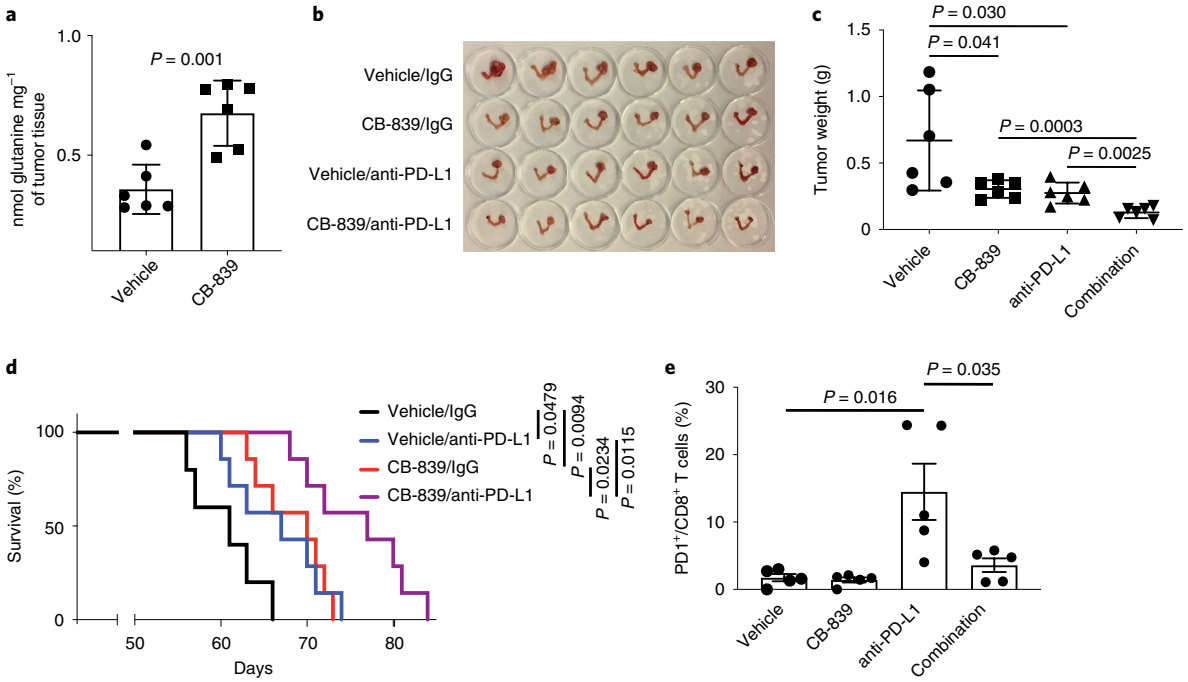

Fig. 6 | GLS inhibition in combination with immune checkpoint blockade suppresses the growth of *Arid1a/Pik3ca* OCCC. a, Glutamine levels in OCCCs developed from the *Arid1a/Pik3ca* genetic mouse model treated with vehicle control or CB-839 ($n=6$ mice per group). **b**,**c**, Mice bearing *Arid1a/Pik3ca* OCCCs were randomized into four indicated treatment groups. Shown are images of reproductive tracts with tumors from indicated groups at end of treatment (**b**). Tumor weight was measured as surrogate for tumor burden (**c**) ($n=6$ mice per group). **d**, After completing treatment, mice were followed for survival and Kaplan–Meier survival curves for each of the indicated groups are shown ($n=7$ mice per group). **e**, At end of treatment, percentage of PD1-positive CD8$^+$ T cells was assessed by flow cytometry in the peritoneal wash, in which tumors had disseminated. Error bars represent mean with s.d. in **a** and **c** and with s.e.m. in **e**. *P* values were calculated using two-tailed Student's *t*-test in **a**, **c**, **e** and log-rank test in **d**.

mine metabolism, *GLS1* is the top significantly upregulated gene that encodes an enzyme that can positively regulate the metabolism of glutamine into aspartate (Extended Data Fig. 4f–h). Together, we conclude that *ARID1A* inactivation creates glutamine dependence through both *GLS1* upregulation and glutamine utilization, such as aspartate generation and nucleotide synthesis.

Clinically applicable GLS inhibitor CB-839 is effective against *ARID1A*-inactivated OCCCs. We next sought to determine the therapeutic potential of GLS inhibitor CB-839 for *ARID1A*-mutated tumors. Toward this goal, we used three different mouse models. First, we used orthotopic xenograft models formed by *ARID1A*-mutated TOV21G OCCC cells. Briefly, orthotopically transplanted cells were allowed to grow for 1 week to establish orthotopic tumors (Extended Data Fig. 5a). Mice were then randomized and treated twice daily for 3 weeks with vehicle control or CB-839 (200 mg kg^{-1} body weight) orally, the same dose as previously reported[34]. We used tumor weight as a surrogate for tumor burden. Notably, CB-839 treatment significantly reduced the burden of orthotopic xenografts formed by *ARID1A*-mutated cells (Fig. 5a,b). This correlated with a significant improvement of survival of tumor-bearing mice (Fig. 5c). Notably, the observed tumor suppressive effect by CB-839 treatment is *ARID1A*-status dependent. For example, CB-839 treatment significantly reduced the burden of orthotopic xenografts formed by *ARID1A* knockout RMG1 cells (Extended Data Fig. 5b). In contrast, CB-839 did not significantly affect growth of tumors formed by *ARID1A* wild-type control RMG1 cells (Extended Data Fig. 5c). Notably, CB-839 significantly reduced expression of cell proliferation marker Ki67 and mitotic marker serine 10 phosphorylated histone H3 (pH3S10) in tumors formed by *ARID1A*-mutated TOV21G or *ARID1A* knockout, but not control wild-type RMG1, cells (Fig. 5d,e and Extended Data Fig. 5d,e). In contrast, expression of apoptosis marker cleaved caspase 3 was not affected by CB-839 treatment (Fig. 5d,e and Extended Data Fig. 5d,e). This is consistent with our in vitro finding that CB-839 significantly reduced S phase of the cell cycle in *ARID1A*-inactivated cells. We next sought to expand these studies into OCCC patient-derived xenografts (PDXs). Consistent with our mechanistic studies, compared with *ARID1A* wild-type OCCC PDX, GLS1 was upregulated in the OCCC PDX harboring a frameshift *ARID1A* mutation (Fig. 5f). Indeed, CB-839 significantly reduced tumor burden in *ARID1A*-mutated, but not *ARID1A* wild-type, OCCC PDXs (Fig. 5g–j). Consistently with previous reports[28], CB-839 was well tolerated in vivo. For example, CB-839 treatment did not affect body weight of treated tumor-bearing mice (Extended Data Fig. 5f). Thus, we conclude that GLS inhibitor CB-839 is effective in *ARID1A*-inactivated OCCCs.

GLS inhibitor synergizes with immune checkpoint blockade in an *ARID1A*-inactivated immunocompetent OCCC model. Lymphocyte function in the tumor microenvironment is regulated by glutamine metabolism[35]. Notably, in a conditional genetic *Arid1a*$^{flox/flox}$ */Pik3ca*^{H1047R} OCCC mouse model as we and others published[25,36], CB-839 treatment significantly increased glutamine levels in treated tumors (Fig. 6a). Consistent with our findings from orthotopic xenograft and PDX models, CB-839 treatment significantly reduced burden in a pre-established genetic OCCC model (Fig. 6b,c). *ARID1A* mutation confers sensitivity to immune checkpoint blockades, such as anti-PD-L1 (refs. [19,21]). In addition, recent evidence shows that glutamine antagonism in effector T cells can be exploited as a 'metabolic checkpoint'[37]. Thus, we examined whether CB-839 synergizes with anti-PD-L1 in the *Arid1a/Pik3ca* immune-competent OCCC genetic mouse model.

Indeed, a combination of CB-839 and anti-PD-L1 was significantly more effective in reducing tumor burden and improving survival of tumor-bearing mice compared with either one of the individual treatments (Fig. 6c,d). Consistent with previous reports[37,38], CB-839 treatment prevented $CD8^+$ T cell exhaustion induced by PD-L1 antibody as evidenced by a decrease in PD1-positive $CD8^+$ T cells (Fig. 6e and Extended Data Fig. 6a). Notably, CB-839 did not affect PD-L1 expression on *ARID1A*-mutated TOV21G cells (Extended Data Fig. 6b). Together, we conclude that clinically applicable GLS inhibitor CB-839 synergizes with immune checkpoint blockade in suppressing the growth of *ARID1A*-inactivated OCCC.

Discussion

Here we show that inactivation of the SWI/SNF complex subunits such as ARID1A creates a dependence on glutamine, which correlates with transcriptional repression of the *GLS1* gene by the SWI/SNF complex. The observed glutamine dependence correlates with an increase in the utilization of glutamine carbon through the TCA cycle to generate aspartate, which is an essential substrate for nucleotide synthesis[39,40]. Consistent with previous reports[33], the observed glutamine dependence was created by both an upregulation of GLS1 and an increase in glutamine utilization, which supports our findings that GLS1 activity is necessary but not sufficient to confer sensitivity to GLS inhibitor CB-839. These findings suggest that ARID1A may also regulate other metabolic pathways that utilize intermediate glutamine metabolites, which together with GLS1 upregulation confers sensitivity to GLS inhibitor. Consistent with our findings, a previous study showed mutation in the SWI/SNF subunit *SMARCA4* in lung cancer enhances oxidative phosphorylation[41]. Interestingly, we show that ARID1A inactivation creates glutamine dependence with a simultaneous decrease in glucose uptake. These findings suggest that inactivation of the SWI/SNF complex reprograms metabolic pathway from glycolysis to glutamine dependence.

Our results show that clinically applicable GLS inhibitor CB-839 can be repurposed for SWI/SNF altered cancers such as *ARID1A*-mutated OCCCs that currently lack effective therapeutic options. This is a personalized therapeutic strategy because *ARID1A* mutation serves as a biomarker, whereas *ARID1A*-repressed *GLS1* serves as *ARID1A* mutation-dependent therapeutic target. A limitation of this approach is that *GLS1* regulation by *ARID1A* is SWI/SNF-complex-dependent. For example, deletion of chr19p, where *SMARCA4* is located, has been reported in OCCCs[7] and our results showed that SMARCA4 inactivation also upregulates *GLS1* and confers sensitivity to CB-839 in both cell lines and primary cultures. In addition, our findings support that a combination of GLS inhibition with immune checkpoint blockade is synergistic in suppressing *ARID1A*-inactivated tumors. The combination is unique in that it leverages both tumor-suppressive effects of GLS inhibition in tumor cells and boosting antitumor immunity in the tumor microenvironment[37]. Notably, GLS inhibitor CB-839 is well tolerated in clinical trials as a single agent and in combination studies[28,29]. In addition, immune checkpoint blockades are US Food and Drug Administration-approved. Thus, the combinatory therapeutic strategy reported here is immediately translatable to potentially benefit patients. Given the fact that ARID1A is the most frequently mutated epigenetic regulator and SWI/SNF is altered in ~20% of all human cancers[1,4,5], we expect our findings to have far-reaching implications in developing urgently needed therapeutic approaches for these tumors.

Methods

Cell lines. OCCC cell line RMG1 cells were cultured in 1:1 Dulbecco's modified Eagle's medium (DMEM)/F12 supplemented with 10% FBS. OCCC cell lines TOV21G, OVCA429, OVISE, SKOV3 and ES2 cells were cultured in RPMI 1640 with 10% FBS and 1% penicillin/streptomycin at 37 °C supplied with 5% CO_2. OCCC cell lines JHOC5, JHOC7 and JHOC9 were purchased from Riken cell bank, OVTOKO and OVMANA cell lines were obtained from JCRB cell bank and IGROV1 cells were obtained from National Cancer Institute cell bank. These cells were cultured in RPMI supplemented with 10% FBS and maintained at 37 °C supplied with 5% CO_2. Rhabdoid tumor cell line G401 cells were cultured in McCoy's 5a medium with 10% FBS and 1% penicillin/streptomycin at 37 °C supplied with 5% CO_2. Renal clear cell cancer lines UMRC2 and RCC4 were cultured in DMEM supplemented with 10% FBS and maintained at 37 °C supplied with 5% CO_2. Viral packing cells 293FT and Phoenix were cultured in DMEM with 10% FBS and 1% penicillin/streptomycin at 37 °C supplied with 5% CO_2. Primary human ovarian clear cell cultures were as described previously[25]. The protocol for using primary cultures of human ovarian clear cell tumor cells was approved by the University of British Columbia Institutional Review Board (H18-01652). Informed consent was obtained from human participants. All relevant ethical regulations have been complied with. Primary tumor cells were cultured in RPMI 1640 supplemented with 10% FBS and 1% penicillin/streptomycin. All cell lines were authenticated using short tandem repeat DNA profiling. Mycoplasma testing was performed using LookOut Mycoplasma PCR detection (Sigma) every month. *ARID1A* knockout RMG1 and OVCA429 cells were generated previously[23].

Plasmids and lentivirus/retrovirus infection. plentiCRISPR v2 (52961) and pMXS-SLC1A3 (72873) were obtained from Addgene. pLKO.1-shARID1A (TRCN0000059090) was purchased from Open Biosystems (RHS3979-201776877). pLKO.1-GLS1-shRNA1 (TRCN0000051134), pLKO.1-GLS1-shRNA1 (TRCN0000051135), pLKO.1-SMARCB1-shRNA1 (TRCN0000039585), pLKO.1-SMARCB1-shRNA2 (TRCN0000039587), pLKO.1-SMARCA4-shRNA1 (TRCN0000015549) and pLKO.1-SMARCA4-shRNA2 (TRCN0000015552) were obtained from the Wistar Institute Molecular Screening and Protein Expression Facility. FUGW V5-GLS1 was obtained from C. van Dang as previously published[32]. HEK293FT/Phoenix cells were transfected by Lipofectamine 2000 for lentivirus package. Lentivirus was collected and filtered with 0.45-μm filter 48 h after transfection. Cells infected with lentivirus/retrovirus were selected in 1 μg ml^{-1} puromycin or 1 μg ml^{-1} blasticidin 48 h after infection.

Colony formation. Cells were seeded in 24-well plates with different numbers according to growth rate. RPMI medium with 10% FBS and 1% penicillin/streptomycin was used for all colony-formation experiments. Medium was changed every 2 d with appropriate drug doses for 10–12 d. Colonies were stained with 0.05% crystal violet. The signal was quantified by intensity using National Institutes of Health ImageJ software.

Western blot. Whole-cell lysate was extracted with RIPA lysis buffer (50 mM Tris (pH 8.0), 150 mM NaCl, 1% Triton X-100, 0.5% sodium deoxycholate, 1 mM EDTA, 1 mM dithiothreitol and 1 mM phenylmethyl sulfonyl fluoride) on ice. Proteins were denatured using 1× SDS loading buffer (50 mM Tris-HCl (pH 6.8), 2% SDS, 10% glycerol, 0.1% bromophenol blue and 10 mM dithiothreitol) and separated by SDS–PAGE and transferred to a PVDF membrane (Millipore). Membranes were blocked with 5% nonfat milk and then incubated with primary antibodies and secondary antibodies.

Antibodies to the following proteins were used in western blots: rabbit anti-ARID1A (Cell Signaling, cat. no. 12354, 1:1,000 dilution for western blot), rabbit anti-SMARCA4 (Cell Signaling, cat. no. 49360, 1:1,000 dilution for western blot), rabbit anti-ARID1B (Abgent, cat. no. AT1190a, 1:1,000 dilution for western blot), rabbit anti-GLS (Abcam, cat. no. 93434, 1:2,000 dilution for western blot), rabbit anti-SNF5 (Bethyl, cat. no. A301-087A, 1:1,000 dilution for western blot), rabbit anti-α-tubulin (Cell Signaling, cat. no. 2125, 1:2,000 dilution for western blot) and mouse anti-β-actin (Sigma, cat. no. A5316, 1:5,000 dilution for western blot).

Metabolite profiling and isotope tracing. LC–MS/MS was performed by the Wistar Proteomics and Metabolomics Facility. For metabolite profiling experiments, cells (2 million per sample) were treated with 1 μM CB-839 for 3 d. Polar metabolites were extracted with 1 ml ice-cold extraction solution (80% LC–MS grade methanol/0.2 μM internal standard mix (Cambridge Isotope, MSK-A2-1.2) in water). After 15 s vortex and 15 min incubation on dry ice, samples were spun down for 15 min at 4 °C at maximum speed. The supernatant was transferred to a new tube and stored at −80 °C. The pellet was used to determine protein concentration. For glutamine tracing experiment, cells were pre-treated with 1 μM CB-839 for 2 d and labeled with fresh 1 mM $^{13}C_5$-L-glutamine for 16 h. Cells were spun down and pellets were resuspended in ice-cold extraction solution containing LC–MS-grade methanol, acetonitrile and ultrapure water at a ratio of 5:3:2 (v/v/v). Samples were vortexed for 5 min at 4 °C before centrifugation. Final cleared metabolite extracts from cells were transferred to silanized glass vials and loaded onto an autosampler for analysis by LC–MS. LC–MS analysis was performed on a Q Exactive HF-X Hybrid Quadrupole-Orbitrap mass spectrometer (Thermo Fisher Scientific) equipped with a HESI II probe and coupled to a Vanquish Horizon UHPLC system (Thermo Fisher Scientific). Then, 2 μl of sample was injected and separated by HILIC chromatography on a ZIC-pHILIC 2.1 mm i.d. × 150 mm column (EMD Millipore). The mobile phase A was 20 mM ammonium carbonate, 0.1% ammonium hydroxide (pH 9.2) and mobile phase B was acetonitrile. LC was run at a flow rate of 0.2 ml min^{-1} and gradient used was as follows: 0 min, 85% B; 2 min, 85% B; 17 min, 20% B; 17.1 min, 85% B; and 26 min, 85% B. The column was maintained at 45 °C and the mobile phase was also pre-heated at 45 °C before

flowing into the column. The relevant MS parameters were as listed: sheath gas, 40; auxiliary gas, 10; sweep gas, 1; auxiliary gas heater temperature, 350 °C; spray voltage, 3.5 kV for the positive mode and 3.2 kV for the negative mode. Capillary temperature was set at 325 °C and funnel RF level at 40. Samples were analyzed in full MS scan with polarity switching at scan range 65 to 975 m/z; 120,000 resolution; automated gain control target of 1E6; and maximum injection time of 100 ms. Identification and quantitation of metabolites was performed using TraceFinder 4.1 and Compound Discoverer 3.0 (Thermo Fisher Scientific).

Metabolite set enrichment analysis. Metabolite level was determined from the MS peak area and normalized to protein concentration. A Student's *t*-test was used to identify difference between two groups. Differential metabolites ($P < 0.1$, fold change >1.3) were used for pathway enrichment analysis. Metabolomic pathways were identified using MSEA v.4.0 (https://www.metaboanalyst.ca/faces/upload/PathUploadView.xhtml). Over representation analysis was utilized for comprehensive screening of affected pathways.

Glucose uptake assay. For glucose uptake assay, cells were seeded in six-well plates to grow at 70% confluence. Regular medium was removed (10% FBS) and cells were incubated in 0.5% FBS medium with 10 μM 2-NBDG (Thermo Fisher Scientific) at 37 °C with 5% CO_2 for the indicated time period. After incubation, cells were collected and washed twice with ice-cold PBS on ice. Samples were analyzed on LSRII flow cytometer (488 nm excitation laser). Mean fluorescence intensity was quantified by FlowJo v.10.0.7 software.

Seahorse mitochondrial fuel dependency. Glutamine dependency was determined according the instruction of Agilent Seahorse XF Mito Fuel Flex Test kit (Agilent). Briefly, cells (RMG1 cells, 20,000 per well; OVCA429 cells, 10,000 per well) were seeded in XF96 Cell Culture Microplate the day before running the assay. The next day, cells were incubated with 180 μl DMEM without FBS at 37 °C in a non-CO_2 incubator for 1 h. Working concentrations of inhibitors used in the glutamine dependency assay are as followed: CB-839 at 5 μM, UK 5099 at 20 μM, etomoxir at 10 μM and rotenone/oligomycin A at 2 μM. The assay was run on Seahorse Bioanalyzer XFe96. Glutamine dependency was calculated by the equation in the manual provided by the manufacturer. Samples were normalized by protein concentration.

GLS activity and glutamine measurement assay. GLS activity was determined using GLS assay kit (Biomedical Research Service). Briefly, 2 million cells were washed with ice-cold PBS and lysed using 100 μl 1× Cell Lysis buffer on ice for 5 min with gentle agitation. Supernatant was collected after centrifugation at maximum for 3 min. Followed by measuring protein concentration, samples were diluted to 0.2–2 mg ml^{-1} and 10 μl was used for GLS assay. Samples were combined with 40 μl fresh glutamine solution and incubated in a humidified 37 °C non-CO_2 incubator for at least 2 h. Followed by adding 50 μl TA assay solution and incubating for another 2 h, the reaction was stopped by adding 50 μl 3% acetic acid. GLS activity was measured by absorbance at OD_{492} using a plate reader (Versamax).

Tumor glutamine levels were determined using Glutamine Assay kit (Colorimetric, Abcam) following the instructions. Briefly, 10–20 mg tumor tissue was washed with cold PBS and resuspended in 10× ice-cold hydrolysis buffer. Tissue was homogenized and centrifuged for 10 min at 4 °C at 10,000*g*. Supernatant was deproteinized by a 10-kD Spin column. Deproteinized samples were used for glutamine detection. Absorbance at 450 nm was measured on a microplate reader.

Quantitative PCR with reverse transcription. Total RNA was extracted using Trizol (Invitrogen) according to the manufacturer's protocol. Extracted RNAs were used for RT–PCR with High-Capacity cDNA Reverse Transcription kit (Thermo Fisher Scientific). Quantitative PCR was performed using QuantStudio 3 Real-Time PCR System. Primers are shown in Supplementary Table 2.

Chromatin immunoprecipitation and CUT&RUN. ChIP was performed as previously described[42]. The following antibodies were used for ChIP: rabbit anti-SNF5 (Bethyl, cat. no. A301-087A, 5 μg per IP), rabbit anti-BAF155 (Abcam, cat. no. ab172638, 2 μg per IP) and mouse anti-Pol II (Santa Cruz, cat. no. sc-47701, 5 μg per IP). Isotype-matched IgGs were used as negative controls. ChIP DNA was purified by Zymo ChIP DNA clean and concentrator kit (Zymo research) and analyzed by qPCR. Primers targeting GLS promoter used for ChIP–qPCR are shown in Supplementary Table 2.

CUT&RUN was performed as described[43] with modifications. In brief, 5 million cells were permeabilized with 0.02% digitonin. Pellets were washed and incubated with antibody buffer containing ARID1A antibody (Abcam, cat. no. ab182560, 1:100 dilution) at 4 °C for at least 15 min with rotation. Followed by washing, the pellets were incubated with 700 ng ml^{-1} pA-MNase (provided by the Henikoff laboratory) at 4 °C for 1 h. Targeting digestion was initiated by adding 100 mM $CaCl_2$ to a final concentration of 2 mM. The digestion was stopped by mixing in 2× STOP solution. Solubilized chromatin fragments were released and purified for qPCR.

Cell cycle analysis. For cell cycle analysis, cells were collected at 40% confluence upon treatment of 1 μM CB-839 for 3 d. After washing with cold PBS, cells were fixed in cold 70% ethanol for at least 1 h at 4 °C. Cells were spun down at 850*g* and washed twice with PBS. Followed by RNase A digestion (work concentration 100 μg ml^{-1}) and PI staining (work concentration 50 μg ml^{-1}) at 37 °C for 15 min, samples were analyzed on LSRII flow cytometer (488 nm excitation laser). Data were acquired using DB FACSDiva v.8.0. Forward scatter and side scatter were used to identify single cells. DNA content was quantified and analyzed by FlowJo v.10.0.7 software.

Immunohistochemistry. IHC staining was performed on consecutive sections from xenografted tumors dissected from immunocompromised NSG female mice as previously described[42]. Staining was performed using antibodies against ARID1A (Cell Signaling, cat. no. 12354, 1:1,000 dilution), GLS1 (Abcam, cat. no.93434, 1:1,000 dilution), Ki67 (Abcam, cat. no. ab16667, 1:500 dilution), cleaved caspase 3 (Cell Signaling, cat. no. 9661, 1:50 dilution) and serine 10 phosphorylated Histone H3 (p-H3S10) (Abcam, cat. no. ab5176, 1:200 dilution). Counterstaining was performed with Mayer's hematoxylin (Dako, cat. no. 3309).

Mouse OCCC models. Protocols were approved by the Institutional Animal Care and Use Committee (IACUC) of the Wistar Institute. Mice were maintained at 22–23 °C with 40–60% humidity and a 12-h light–12-h dark cycle. The number of mice used in vivo was determined by results from in vitro experiments. The intrabursal model was performed as described[25]. Briefly, 1×10^6 cells were unilaterally injected into the ovarian bursa sac of 6–8-week-old female NSG mice. For orthotopic xenografts formed by TOV21G, 1 week after injection, tumor-bearing mice were randomized into two groups ($n = 6$ per group). Mice in each group were orally treated with vehicle (25% (w/v) hydroxypropyl-β-cyclodextrin (HPBCD) in 10 mM citrate, pH 2) and 200 mg kg^{-1} CB-839 twice daily for 3 weeks. For orthotopic xenografts formed by RMG1 or *ARID1A* knockout RMG1 cells, mice were randomized into two groups ($n = 7$ per group) 1 week after injection and orally treated with vehicle (25% (w/v) HPBCD in 10 mM citrate, pH 2) and 200 mg kg^{-1} CB-839 twice daily for 3 weeks. Tumors were surgically dissected and tumor burden was calculated on the basis of tumor weight. Analysis was performed blindly but not randomly. The Wistar Institute IACUC guideline was followed in determining the time for ending survival experiments (such as when tumor burden >10% of body weight).

For PDX xenograft models, passage 3 of previously described[44] *ARID1A* wild-type and mutated PDXs were transplanted to the ovarian bursa sac of 6–8-week-old female NSG mice. Mice were randomized into four groups 1 month after transplantation and orally treated with vehicle (25% (w/v) HPBCD in 10 mM citrate, pH 2) or 200 mg kg^{-1} CB-839 twice daily for 3 weeks. Mice bearing *ARID1A*-mutant PDXs were fed with aspartic-acid-free diet due to the high expression of aspartate transporter in the tumor. Tumors were surgically dissected and tumor burden was calculated on the basis of tumor weight.

For *Arid1a*$^{-/-}$/*Pik3ca*^{H1047R} genetic OCCC mouse model, intrabursal adenovirus-Cre injection was used to induce OCCC formation in 6–8-week-old female mice. Mice were randomized into six groups 4 weeks after injection. Mice were randomized into the following four treatment groups: vehicle and IgG control, CB-839 (200 mg kg^{-1} twice daily, orally) and IgG control, vehicle control and anti-PD-L1 (10 mg kg^{-1}, twice a week, intraperitoneally) and a combination of CB-839 and anti-PD-L1. At the end of treatment, mice were killed and tumors were surgically dissected. Tumor burden was calculated on the basis of tumor weight. The survival experiment was performed following The Wistar Institute IACUC guideline (tumor burden >10% of body weight).

Immune cell profiling was analyzed as we previously described[19]. Briefly, tumor cells were extracted using Mouse Dissociation kit (Miltenyi Biotec, cat. no. 130-096-730) according to the manufacturer's instructions. The cells were then mashed with 70-μM strainer and used for staining. For peritoneal wash, peritoneal cavity of mice was washed three times with 5 ml PBS and incubated in RBC lysis buffer (Thermo Fisher Scientific, cat. no. 00-4333-57). Live/dead cells were discriminated by Zombie Yellow Fixable Viability kit (BioLegend, cat. no. 423103). Cell surface staining was performed using antibodies against CD3e (BD, cat. no. 552774, 1:1,000 dilution), CD45 (BioLegend, cat. no. 103147, 1: 1,000 dilution), CD4 (BioLegend, cat. no. 100516, 1:1,000 dilution), CD8a (BioLegend, cat. no. 100708, 1:1000 dilution), CD69 (BioLegend, cat. no. 104510, 1:1,000 dilution), PD1 (BioLegend, cat. no. 109109, 1:1,000 dilution) and PD-L1 (BioLegend, cat. no. 124321, 1:1,000 dilution). Data were acquired using LSRII-18 and analyzed using FlowJo software.

Statistics and reproducibility. Statistical analysis was performed using GraphPad Prism 7 (GraphPad). Analysis of variance with Fisher's least significant difference was used to identify significant differences in multiple comparisons. Spearman correlation analysis was used to examine the correlation between two factors. Log-rank test was used to compare the survival distributions among experimental groups. Experiments were repeated at least twice. Quantitative data are expressed as mean ± s.d. unless otherwise stated. No statistical method was used to predetermine sample size. No data were excluded from the analyses. All analysis was performed blindly but not randomly. Animal experiments were randomized.

Reporting Summary. Further information on research design is available in the Nature Research Reporting Summary linked to this article.

Data availability

The previously published ChIP-seq data that were re-analyzed here are available in the Gene Expression Omnibus under accession codes GSE120060 (ref. [45]), GSE69566 (ref. [46]), GSE124225 (ref. [47]) and GSE123284 (ref. [48]). Previously published RNA-seq data that were re-analyzed here are available under accession codes GSE106665 (ref. [49]) and GSE124227 (ref. [47]). Previously published ATAC-seq data that were re-analyzed here are available under accession codes GSE124224 (ref. [47]), GSE106665 (ref. [49]) and GSE101966 (ref. [50]). Metabolomics data have been deposited into MassIVE under accession code MSV000086347. Cancer Cell Line Encyclopedia RNA-seq data were downloaded from https://portals.broadinstitute.org/ccle/data/. Human lung adenocarcinoma, renal clear cell carcinoma, skin cutaneous melanoma and uterine corpus endometrial carcinoma data were derived from https://www.cbioportal.org/. Source data for unprocessed immunoblots for Figs. 1c, 2b,e–j and 3a,f and Extended Data Figs. 1a,b, 2f,h and 3f and source data used for statistical analyses have been provided as Source Data files. All other data supporting the findings of this study are available from the corresponding author on reasonable request. Source data are provided with this paper.

Received: 26 December 2019; Accepted: 25 November 2020;
Published online: 11 January 2021

References

1. Kadoch, C. & Crabtree, G. R. Mammalian SWI/SNF chromatin remodeling complexes and cancer: mechanistic insights gained from human genomics. *Sci. Adv.* **1**, e1500447 (2015).
2. Wilson, B. G. & Roberts, C. W. SWI/SNF nucleosome remodellers and cancer. *Nat. Rev. Cancer* **11**, 481–492 (2011).
3. Fukumoto, T., Magno, E. & Zhang, R. SWI/SNF complexes in ovarian cancer: mechanistic insights and therapeutic implications. *Mol. Cancer Res.* **16**, 1819–1825 (2018).
4. Bailey, M. H. et al. Comprehensive characterization of cancer driver genes and mutations. *Cell* **173**, 371–385 (2018).
5. Lawrence, M. S. et al. Discovery and saturation analysis of cancer genes across 21 tumour types. *Nature* **505**, 495–501 (2014).
6. Jones, S. et al. Frequent mutations of chromatin remodeling gene ARID1A in ovarian clear cell carcinoma. *Science* **330**, 228–231 (2010).
7. Murakami, R. et al. Exome sequencing landscape analysis in ovarian clear cell carcinoma shed light on key chromosomal regions and mutation gene networks. *Am. J. Pathol.* **187**, 2246–2258 (2017).
8. Wiegand, K. C. et al. ARID1A mutations in endometriosis-associated ovarian carcinomas. *N. Engl. J. Med.* **363**, 1532–1543 (2010).
9. Mackay, H. J. et al. Prognostic relevance of uncommon ovarian histology in women with stage III/IV epithelial ovarian cancer. *Int. J. Gynecol. Cancer* **20**, 945–952 (2010).
10. Penson, R. T., Dizon, D. S. & Birrer, M. J. Clear cell cancer of the ovary. *Curr. Opin. Oncol.* **25**, 553–557 (2013).
11. Zhang, J., Pavlova, N. N. & Thompson, C. B. Cancer cell metabolism: the essential role of the nonessential amino acid, glutamine. *EMBO J.* **36**, 1302–1315 (2017).
12. Curthoys, N. P. & Watford, M. Regulation of glutaminase activity and glutamine metabolism. *Annu. Rev. Nutr.* **15**, 133–159 (1995).
13. Consortium, G. T. Human genomics. The Genotype-Tissue Expression (GTEx) pilot analysis: multitissue gene regulation in humans. *Science* **348**, 648–660 (2015).
14. Cassago, A. et al. Mitochondrial localization and structure-based phosphate activation mechanism of glutaminase C with implications for cancer metabolism. *Proc. Natl Acad. Sci. USA* **109**, 1092–1097 (2012).
15. Jelinic, P. et al. Immune-active microenvironment in small cell carcinoma of the ovary, hypercalcemic type: rationale for immune checkpoint blockade. *J. Natl Cancer Inst.* https://doi.org/10.1093/jnci/djx277 (2018).
16. Miao, D. et al. Genomic correlates of response to immune checkpoint therapies in clear cell renal cell carcinoma. *Science* **359**, 801–806 (2018).
17. Pan, D. et al. A major chromatin regulator determines resistance of tumor cells to T cell-mediated killing. *Science* **359**, 770–775 (2018).
18. Anagnostou, V. et al. Multimodal genomic features predict outcome of immune checkpoint blockade in non-small-cell lung cancer. *Nat. Cancer* **1**, 99–111 (2020).
19. Fukumoto, T. et al. HDAC6 inhibition synergizes with anti-PD-L1 therapy in ARID1A-inactivated ovarian cancer. *Cancer Res.* https://doi.org/10.1158/0008-5472.CAN-19-1302 (2019).
20. Abou Alaiwi, S. et al. Mammalian SWI/SNF complex genomic alterations and immune checkpoint blockade in solid tumors. *Cancer Immunol. Res.* https://doi.org/10.1158/2326-6066.CIR-19-0866 (2020).
21. Shen, J. et al. ARID1A deficiency promotes mutability and potentiates therapeutic antitumor immunity unleashed by immune checkpoint blockade. *Nat. Med.* https://doi.org/10.1038/s41591-018-0012-z (2018).
22. Hamanishi, J. et al. Safety and antitumor activity of anti-PD-1 antibody, nivolumab, in patients with platinum-resistant ovarian cancer. *J. Clin. Oncol.* **33**, 4015–4022 (2015).
23. Bitler, B. G. et al. Synthetic lethality by targeting EZH2 methyltransferase activity in ARID1A-mutated cancers. *Nat. Med.* **21**, 231–238 (2015).
24. Guan, B., Wang, T. L. & Shih Ie, M. ARID1A, a factor that promotes formation of SWI/SNF-mediated chromatin remodeling, is a tumor suppressor in gynecologic cancers. *Cancer Res.* **71**, 6718–6727 (2011).
25. Bitler, B. G. et al. ARID1A-mutated ovarian cancers depend on HDAC6 activity. *Nat. Cell Biol.* **19**, 962–973 (2017).
26. Labuschagne, C. F., Zani, F. & Vousden, K. H. Control of metabolism by p53 - Cancer and beyond. *Biochim. Biophys. Acta Rev. Cancer* **1870**, 32–42 (2018).
27. Ghandi, M. et al. Next-generation characterization of the cancer cell line encyclopedia. *Nature* **569**, 503–508 (2019).
28. Xu, X. et al. Overview of the development of glutaminase inhibitors: achievements and future directions. *J. Med. Chem.* **62**, 1096–1115 (2019).
29. Eads, J. R. et al. Phase I clinical trial of the glutaminase inhibitor CB-839 plus capecitabine in patients with advanced solid tumors. *J. Clin. Oncol.* https://doi.org/10.1200/JCO.2018.36.15_suppl.2562 (2018).
30. Okazaki, A. et al. Glutaminase and poly(ADP-ribose) polymerase inhibitors suppress pyrimidine synthesis and VHL-deficient renal cancers. *J. Clin. Invest.* **127**, 1631–1645 (2017).
31. McDonald, E. R. 3rd et al. Project DRIVE: a compendium of cancer dependencies and synthetic lethal relationships uncovered by large-scale, deep RNAi screening. *Cell* **170**, 577–592 (2017).
32. Xiang, Y. et al. Targeted inhibition of tumor-specific glutaminase diminishes cell-autonomous tumorigenesis. *J. Clin. Invest.* **125**, 2293–2306 (2015).
33. Daemen, A. et al. Pan-cancer metabolic signature predicts co-dependency on glutaminase and de novo glutathione synthesis linked to a high-mesenchymal cell state. *Cell Metab.* **28**, 383–399 (2018).
34. Gross, M. I. et al. Antitumor activity of the glutaminase inhibitor CB-839 in triple-negative breast cancer. *Mol. Cancer Ther.* **13**, 890–901 (2014).
35. Buck, M. D., O'Sullivan, D. & Pearce, E. L. T cell metabolism drives immunity. *J. Exp. Med.* **212**, 1345–1360 (2015).
36. Chandler, R. L. et al. Coexistent ARID1A-PIK3CA mutations promote ovarian clear-cell tumorigenesis through pro-tumorigenic inflammatory cytokine signalling. *Nat. Commun.* **6**, 6118 (2015).
37. Leone, R. D. et al. Glutamine blockade induces divergent metabolic programs to overcome tumor immune evasion. *Science* **366**, 1013–1021 (2019).
38. Nabe, S. et al. Reinforce the antitumor activity of CD8(+) T cells via glutamine restriction. *Cancer Sci.* **109**, 3737–3750 (2018).
39. Lane, A. N. & Fan, T. W. Regulation of mammalian nucleotide metabolism and biosynthesis. *Nucleic Acids Res.* **43**, 2466–2485 (2015).
40. Zhu, J. & Thompson, C. B. Metabolic regulation of cell growth and proliferation. *Nat. Rev. Mol. Cell Biol.* **20**, 436–450 (2019).
41. Lissanu Deribe, Y. et al. Mutations in the SWI/SNF complex induce a targetable dependence on oxidative phosphorylation in lung cancer. *Nat. Med.* **24**, 1047–1057 (2018).
42. Wu, S. et al. SWI/SNF catalytic subunits' switch drives resistance to EZH2 inhibitors in ARID1A-mutated cells. *Nat. Commun.* **9**, 4116 (2018).
43. Skene, P. J., Henikoff, J. G. & Henikoff, S. Targeted in situ genome-wide profiling with high efficiency for low cell numbers. *Nat. Protoc.* **13**, 1006–1019 (2018).
44. Zhao, B. et al. ARID1A promotes genomic stability through protecting telomere cohesion. *Nat. Commun.* **10**, 4067 (2019).
45. Wu, S. et al. ARID1A spatially partitions interphase chromosomes. *Sci. Adv.* **5**, eaaw5294 (2019).
46. Raab, J. R., Resnick, S. & Magnuson, T. Genome-wide transcriptional regulation mediated by biochemically distinct SWI/SNF complexes. *PLoS Genet.* **11**, e1005748 (2015).
47. Xu, G. et al. ARID1A determines luminal identity and therapeutic response in estrogen-receptor-positive breast cancer. *Nat. Genet.* **52**, 198–207 (2020).
48. Nagarajan, S. et al. ARID1A influences HDAC1/BRD4 activity, intrinsic proliferative capacity and breast cancer treatment response. *Nat. Genet.* **52**, 187–197 (2020).
49. Suryo Rahmanto, Y. et al. Inactivation of ARID1A in the endometrium is associated with endometrioid tumorigenesis through transcriptional reprogramming. *Nat. Commun.* **11**, 2717 (2020).
50. Kelso, T. W. R. et al. Chromatin accessibility underlies synthetic lethality of SWI/SNF subunits in ARID1A-mutant cancers. *eLife* https://doi.org/10.7554/eLife.30506 (2017).

Acknowledgements

We thank Z. Stine and C. Simon from the University of Pennsylvania for UMRC2 and RCC4 cell lines. This work was supported by US National Institutes of Health grants (R01CA160331, R01CA163377, R01CA202919, R01CA239128 and P01AG031862 to R. Z.; P50CA228991 to R. Z. and R.D.; K99CA241395 to S.K.; R50CA221838 to H.-Y.T., S10OD023658 and S10OD023586 to D.W.S.; R01CA195670 to D.G.H., F31CA247336 to J.Z. and T32CA009191 to T.N.) and US Department of Defense (OC180109 and OC190181 to R. Z.). The Honorable Tina Brozman Foundation for Ovarian Cancer Research and the Tina Brozman Ovarian Cancer Research Consortium 2.0 (to R.Z. and R.D.) and Ovarian Cancer Research Alliance (Collaborative Research Development Grant no. 596552 to R.Z. and Ann and Sol Schreiber Mentored Investigator Awards no.

598026 to S.W. and no. 649658 to J.L.). Support of Core Facilities was provided by Cancer Centre Support Grant CA010815 to The Wistar Institute.

Author contributions

S.W., T.F., J.L., T.N., Y.W., D.O., H.L., N.F., J.A.Z., S.K., W.Z., H.-Y. T. and Z.T.S. performed the experiments and analyzed data. S.W., C.V.D. and R.Z. designed the experiments. Q.L. and A.V.K. performed statistical analysis. L.E.S. and R.D. contributed key experimental materials. D.H., D.W.S. and R.Z. supervised studies. S.W, Y.W., D.W.S., Z.T.S., C.V.D. and R.Z. wrote the manuscript. R.Z. conceived the study.

Competing interests

The authors declare no competing interests.

Additional information

Extended data is available for this paper at https://doi.org/10.1038/s43018-020-00160-x.

Supplementary information is available for this paper at https://doi.org/10.1038/s43018-020-00160-x.

Correspondence and requests for materials should be addressed to R.Z.

Peer review information Nature Cancer thanks Steven de Jong and the other, anonymous, reviewer(s) for their contribution to the peer review of this work.

Reprints and permissions information is available at www.nature.com/reprints.

Publisher's note Springer Nature remains neutral with regard to jurisdictional claims in published maps and institutional affiliations.

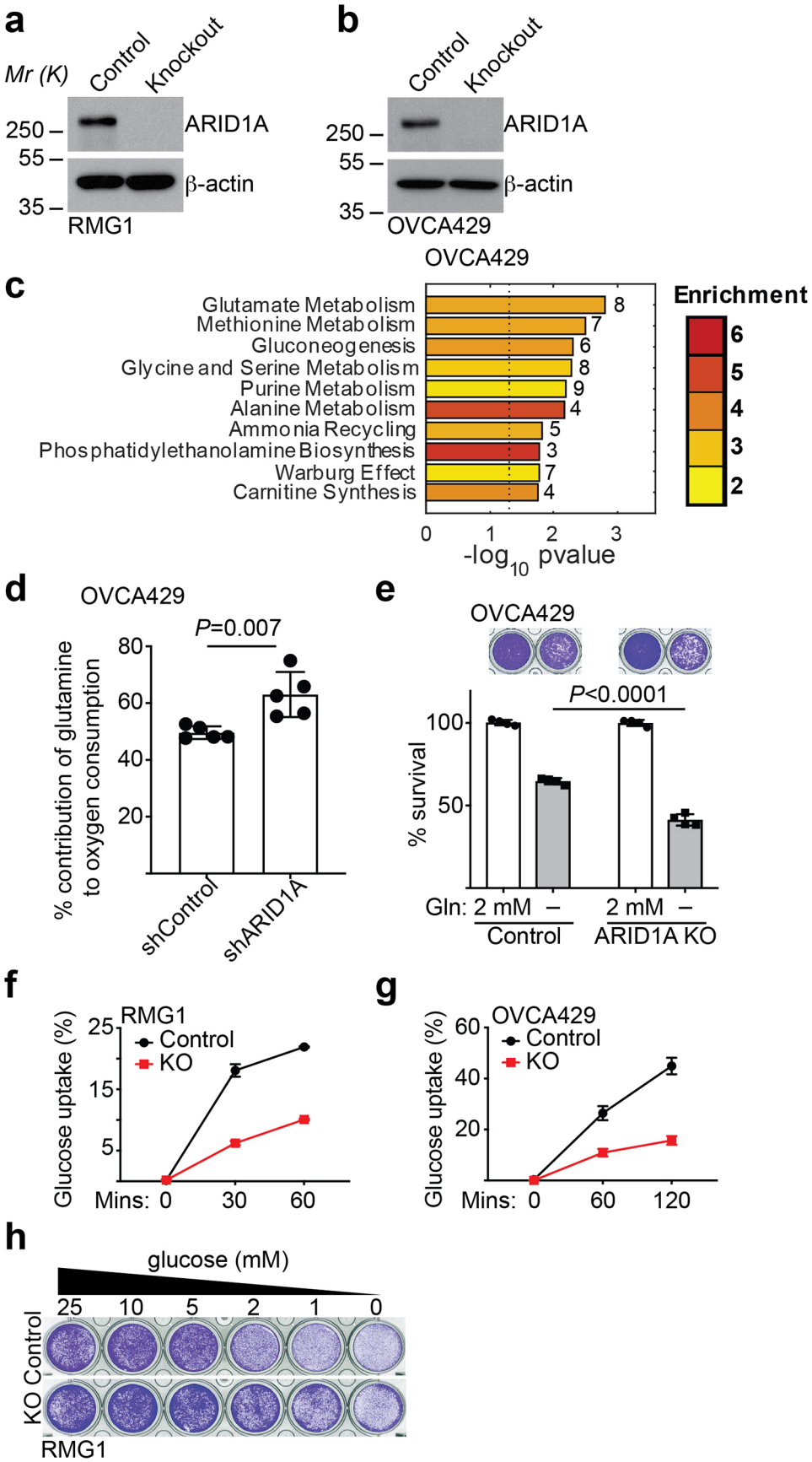

Extended Data Fig. 1 | See next page for caption.

Extended Data Fig. 1 | ARID1A inactivation creates a dependence on glutamine. a-b, Validation of ARID1A knockout in parental and ARID1A knockout RMG1 (**a**) and OVCA429 (**b**) cells. Immunoblots are representative of three independent experiments with similar results. **c**, Top 10 metabolic pathways enriched by ARID1A knockout in OVCA429 cells determined by metabolites set enrichment analysis (MSEA). **d**, Contribution of glutamine to oxygen consumption in the indicated OVCA429 cells expressing shARID1A or control analyzed by Seahorse. n= 5 independent experiments. **e**, Colony formation and quantification of parental and ARID1A knockout OVCA429 cells with or without glutamine deprivation for 12 days. n= 4 independent experiments. **f-g**, A fluorescence glucose analog 2-NBDG-based glucose uptake assayed by flow cytometry analysis for the indicated parental and ARID1A knockout RMG1 (**f**) or OVCA429 (**g**) cells. n= 4 independent experiments. **h**, Colony formation of parental and ARID1A knockout RMG1 cells cultured in the medium with indicated concentration of glucose for 12 days. Shown are representative images of four independent experiments. Error bars represent mean with s.d. in **d**, **e**, **f** and **g**. *P* values were calculated using two-tailed Student *t*-test in **d**, **e** and Fisher's least significant difference test in **c**.

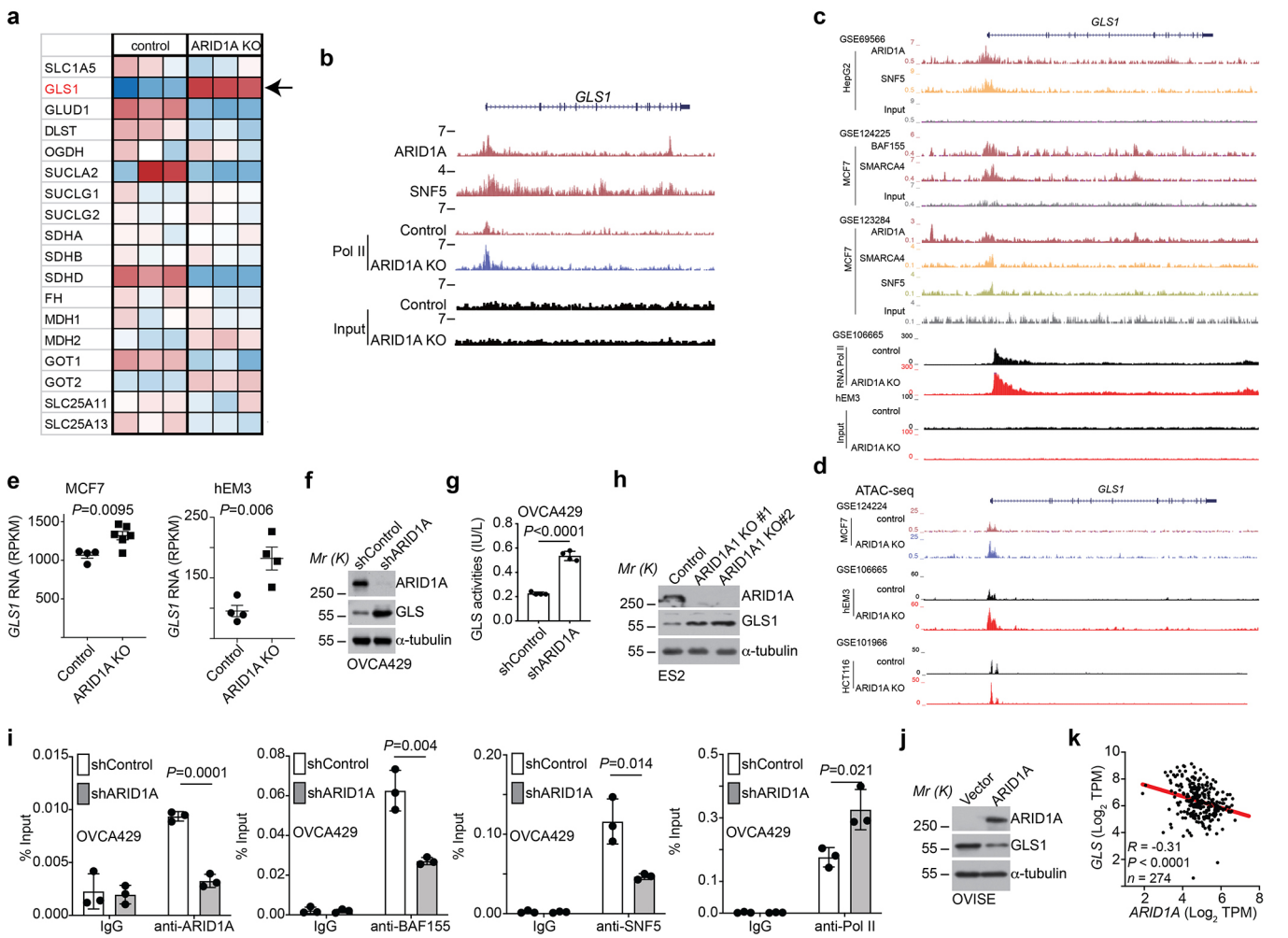

Extended Data Fig. 2 | *GLS1* is a direct target of the SWI/SNF complex. a, Expression of glutamine metabolism related genes in control and ARID1A knockout RMG1 cells determined by RNA-seq analysis. Note that GLS1 shows the highest upregulation in response to ARID1A knockout. n=3 independent experiments. **b**, The indicated ChIP-seq and input tracks in the *GLS1* gene locus in parental and ARID1A knockout RMG1 cells in previously published datasets (GSE120060). **c**, The indicated ChIP-seq and input tracks in the *GLS1* gene locus in the indicated cancer cells based on the public database mining (GSE69566, GSE124225, GSE123284 and GSE106665). **d**, ATAC-seq tracks in the *GLS1* gene locus in parental and ARID1A knockout cells based on the indicated datasets (GSE124224, GSE106665 and GSE101966). **e**, Expression of *GLS1* mRNA in the indicated cancer cells based on based on mining public databases (GSE124227 and GSE106665). **f-g**, Control and ARID1A knockdown OVCA429 cells were examined for expression of ARID1A and GLS1 by immunoblot (**f**) or measured for glutaminase activity (**g**). n= 4 independent experiments. **h**, Control and ARID1A knockout ES2 cells were examined for expression of ARID1A and GLS1 by immunoblot. **i**, The association of ARID1A, BAF155, SNF5 and RNA Pol II with the *GLS1* gene promoter in parental and ARID1A knockdown OVCA429 cells was examined by ChIP-qPCR analysis. An isotype matched IgG was used as a control. n = 3 independent experiments. **j**, Control and wildtype ARID1A ectopically expressing OVISE cells were examined for expression of ARID1A and GLS1 by immunoblot. **k**, Inverse correlation between *GLS1* and *ARID1A* expression in 274 *TP53* wildtype cancer cell lines across cancer types in the Cancer Cell Line Encyclopedia RNAseq database. Immunoblots are representative of three independent experiments with similar results in **f**, **h** and **j**. Error bars represent mean with s.d. in **e**, **g** and **i**. *P* value was calculated using two-tailed Student *t*-test in **e**, **g**, **i** and Spearman correlation analysis in **k**.

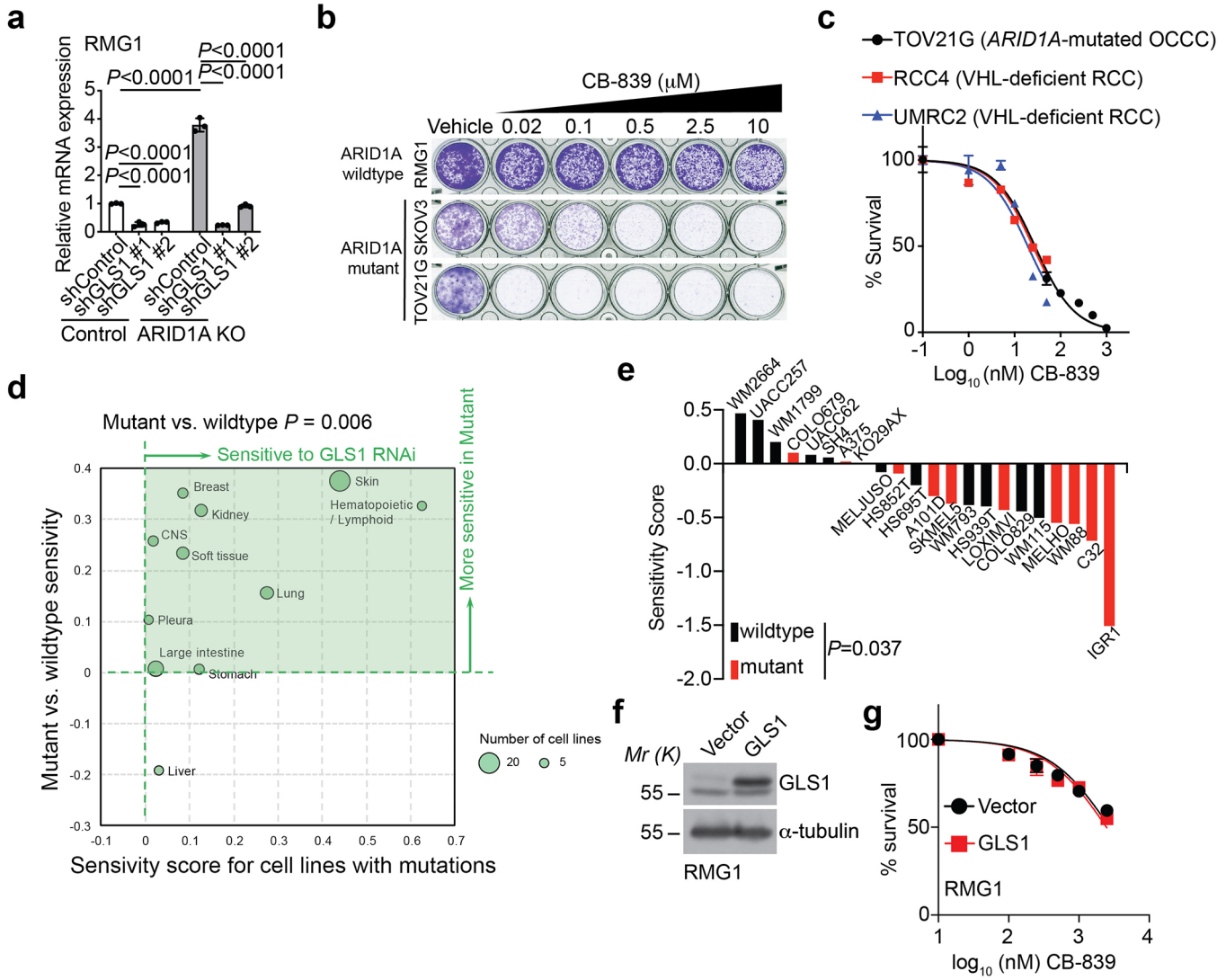

Extended Data Fig. 3 | Inactivation of SWI/SNF complex sensitizes cells to glutaminase inhibition. a, Validation of *GLS1* knockdown by qRT-PCR in parental and ARID1A knockout RMG1 cells expressing the indicated shGLS1s or control. n= 3 independent experiments. **b**, Colony formation by the indicated cells treated with the indicated doses of CB-839. Shown are representative images of 4 independent experiments with similar results. **c**, Dose response curves to glutaminase inhibitor CB-839 determined by colony formation assay in the indicated *ARID1A*-mutated OCCC and VHL-deficient renal clear cell carcinoma (RCC) cell lines. n=4 independent experiments. **d**, Differential sensitivity of *TP53* wildtype cell lines for the indicated cancer types with SWI/SNF wildtype or mutation to *GLS1* knockdown in the Project Achilles dataset. Specifically, *GLS1* shRNA sensitivity score for 384 cell lines along with mutation status of member of SWI/SNF complex (*ARID1A, ARID1B, SMARCA2, PHF10, SMARCA4, SMARCB1, SMARCC1, SMARCC2, SMARCD3, DPF2, ACTL6A*) and *TP53* were downloaded from Broad Cancer Cell Line Encyclopedia database. Only 118 cells lines with wildtype *TP53* were taken for analysis. Cell lines were grouped by source tissue site and categorized into mutant (at least one mutation in any members of SWI/SNF complex) and wildtype SWI/SNF complex groups. Average sensitivity scores to *GLS1* RNAi for each tissue and SWI/SNF complex groups were calculated. Average mutant SNI/SNF scores were plotted versus difference between mutant and wildtype SWI/SNF complex on a bubble plot to illustrate cancer types with association between GLS1 RNAi and SWI/SNF mutation. Size of the data circles were proportional to the number of cells lines in the tissue group. Note that the criteria for including in the analysis is with minimal 5 cell lines in the database. **e**, Sensitivity score of SWI/SNF wildtype or mutated skin cancer cell lines with wildtype *TP53* to *GLS1* knockdown in the Project Achilles dataset. **f-g**, Expression of GLS1 in control and GLS1 ectopically expressed *ARID1A* wildtype RMG1 cells determined by immunoblot (**f**). And the indicated cells were subjected to dose response curves to glutaminase inhibitor CB-839 determined by colony formation assay (**g**). n=4 independent experiments. Immunoblots are representative of two independent experiments with similar results in **f**. Error bars represent mean with s.d. in **a**, **c**, **e** and **g**. *P* values were calculated using two-tailed Student *t*-test in **a**, **e** and one-tailed Student *t*-test in **d**.

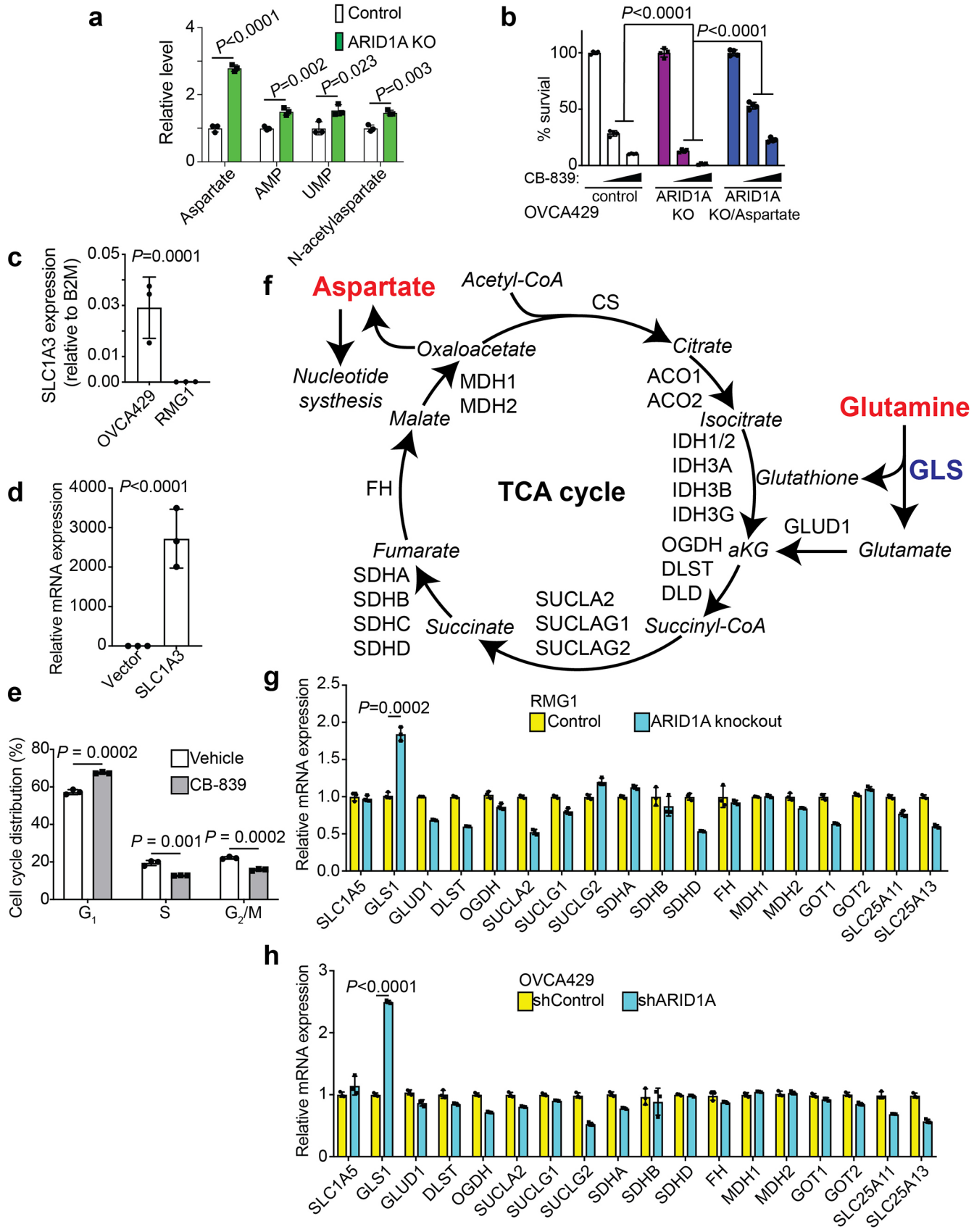

Extended Data Fig. 4 | See next page for caption.

Extended Data Fig. 4 | ARID1A inactivation increases glutamine-dependent aspartate biosynthesis. a, Quantification the indicated metabolites determined by glutamine tracing in control and ARID1A knockout RMG1 cells. n= 3 independent experiments. **b**, Quantification of colony formation by parental or ARID1A knockout OVCAR429 cells cultured in medium supplemented with or without 5 mM aspartate treated with or without CB-839 (0.1 μM or 0.25 μM). n= 4 independent experiments. **c**, Expression of *SLC1A3* in RMG1 and OVCA429 cells determined by qRT-PCR analysis. n= 3 independent experiments. **d**, Expression of *SLC1A3* in ARID1A knockout RMG1 cells with or without ectopic SLC1A3 expression determined by qRT-PCR analysis. n= 3 independent experiments. **e**, Cell cycle distribution in RMG1 ARID1A KO cells treated with or without 1 μM CB-839 for 72 hrs determined by flow cytometry analysis. n= 3 independent experiments. **f**, Schematic of glutamine-dependent aspartate biogenesis through the TCA cycle. **g-h**, Relative expression of genes encoding for enzymes that contribute to aspartate biogenesis from glutamine through the TCA cycle determined by qRT-PCR analysis in parental control and ARID1A knockout RMG1 cells (**g**) or OVCA429 cells with or without ARID1A knockdown (**h**) cells. Validation of 3 independent experiments as shown in Extended Data Fig. 2a. Error bars represent mean with s.d. in **a**, **b**, **c**, **d**, **e**, **g** and **h**. *P* values were calculated using two-tailed Student *t*-test in **a**, **b**, **c**, **d**, **e**, **g** and **h**.

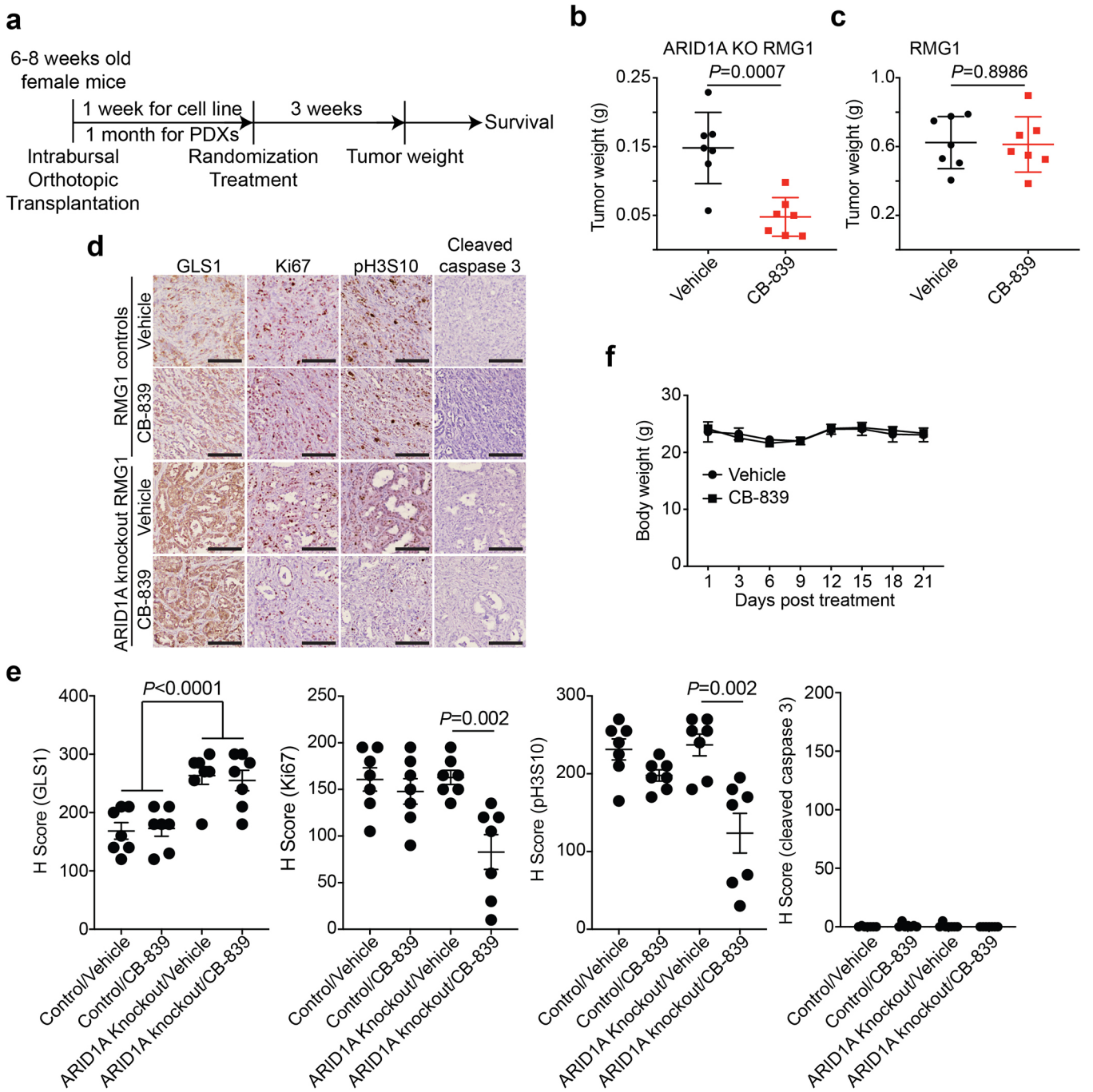

Extended Data Fig. 5 | Glutaminase inhibitor CB-839 suppresses the growth of ARID1A-inactivated OCCCs in vivo. a, Schematic of experimental design and reference time of the mouse experiment. Cells were orthotopically transplanted into non-obese diabetic/severe combined immunodeficiency gamma (NSG) mice and allowed to establish for one week. After the tumors presented palpable masses, the mice were randomized into various treatment groups and treated for an additional three weeks. At the end of treatment of three weeks, mice from various treatment groups were euthanized for measuring tumor weight as a surrogate for tumor burden or followed for survival experiment. **b-c**, Orthotopic xenografts formed by ARID1A knockout (**b**) or control RMG1 cells (**c**) were treated with vehicle or CB-839 for 3 weeks (n=7 mice/group). At the end of the treatment, tumor weight was measured as surrogate for tumor burden. **d-e**, Tumors dissected from b-c, were subjected to immunological staining for GLS1, cell proliferation marker Ki67, mitotic marker serine 10 phosphorylated histone H3 (pH3S10) or apoptosis marker cleaved caspase 3 on serial sections (**d**) and the histological score (H-score) of the indicated markers was quantified from three separate fields from seven tumors from seven individual mice in each of the indicated treatment groups (**e**). Scale bar = 100 μm. **f**, Orthotopic xenografts formed by *ARID1A*-mutated TOV21G cells were treated with vehicle or CB-839 for three weeks (n=6 mice/group). Body weight of tumor bearing mice was measured at the indicated time point. Error bars represent mean with s.d. in **b**, **c, e** and **f**. *P* values were calculated using two-tailed Student *t*-test in **b**, **c** and **e**.

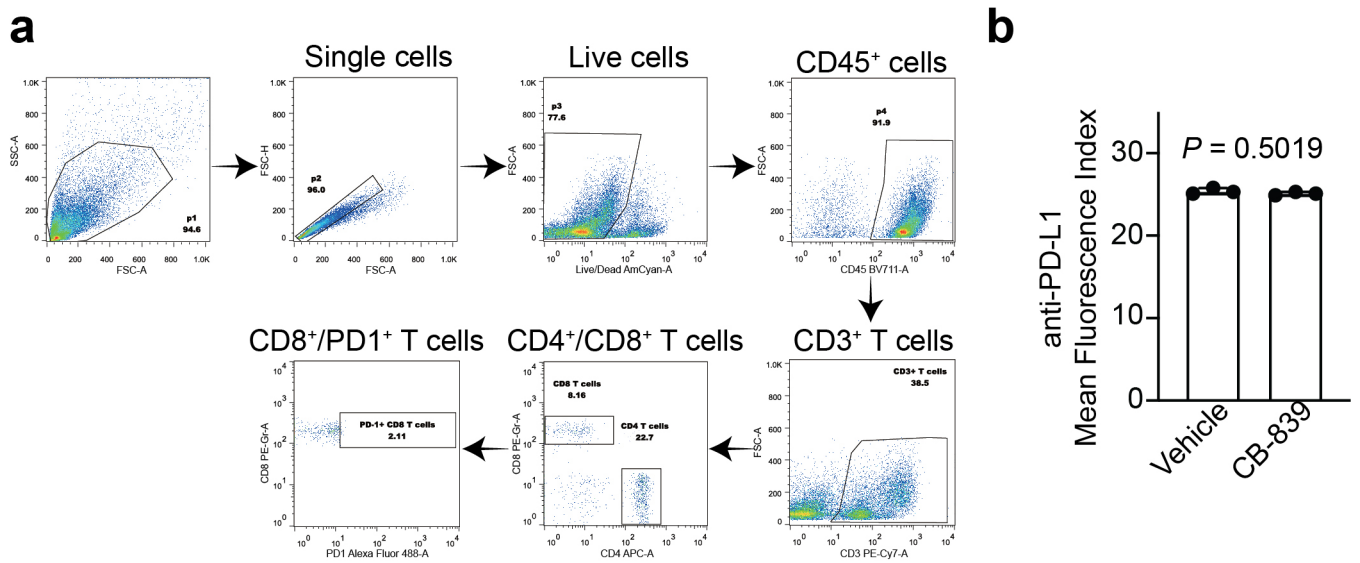

Extended Data Fig. 6 | CB-839 does not affect PDL1 expression. a, The gating strategy used for determining the percentage of PD1$^+$/CD8$^+$ T cell populations. **b**, *ARID1A*-mutated TOV21G cells were treated with vehicle or CB-839 (100 nM) for 48 hours and expression of PDL1 was examined by flow cytometry analysis. n = 3 independent experiments. Error bars represent mean with s.d. in **b**. *P* values were calculated using two-tailed Student *t*-test in **b**.

nature research

Corresponding author(s): Rugang Zhang

Last updated by author(s): Oct 25, 2020

Reporting Summary

Nature Research wishes to improve the reproducibility of the work that we publish. This form provides structure for consistency and transparency in reporting. For further information on Nature Research policies, see Authors & Referees and the Editorial Policy Checklist.

Statistics

For all statistical analyses, confirm that the following items are present in the figure legend, table legend, main text, or Methods section.

n/a	Confirmed	
☐	☒	The exact sample size (*n*) for each experimental group/condition, given as a discrete number and unit of measurement
☐	☒	A statement on whether measurements were taken from distinct samples or whether the same sample was measured repeatedly
☐	☒	The statistical test(s) used AND whether they are one- or two-sided *Only common tests should be described solely by name; describe more complex techniques in the Methods section.*
☒	☐	A description of all covariates tested
☒	☐	A description of any assumptions or corrections, such as tests of normality and adjustment for multiple comparisons
☐	☒	A full description of the statistical parameters including central tendency (e.g. means) or other basic estimates (e.g. regression coefficient) AND variation (e.g. standard deviation) or associated estimates of uncertainty (e.g. confidence intervals)
☐	☒	For null hypothesis testing, the test statistic (e.g. *F*, *t*, *r*) with confidence intervals, effect sizes, degrees of freedom and *P* value noted *Give P values as exact values whenever suitable.*
☒	☐	For Bayesian analysis, information on the choice of priors and Markov chain Monte Carlo settings
☒	☐	For hierarchical and complex designs, identification of the appropriate level for tests and full reporting of outcomes
☒	☐	Estimates of effect sizes (e.g. Cohen's *d*, Pearson's *r*), indicating how they were calculated

Our web collection on statistics for biologists contains articles on many of the points above.

Software and code

Policy information about availability of computer code

Data collection	Identification and quantification of metabolites was performed using TraceFinder 4.1 and Compound Discoverer 3.0 (Thermo Fisher). Flow cytomertry data were acquired using BD FACSDiva Version 8.0.
Data analysis	Prism 7 for Mac was used for calculating p values. Metabolomic pathways were identified using Metabolite Set Enrichment Analysis (MSEA version 4.0) (available at https://www.metaboanalyst.ca/faces/upload/PathUploadView.xhtml). Flow cytometry results were analyzed using FlowJo v10.0.7 software. The intensity of colony formation was quantified by Mac OS X version of NIH Image J software.

For manuscripts utilizing custom algorithms or software that are central to the research but not yet described in published literature, software must be made available to editors/reviewers. We strongly encourage code deposition in a community repository (e.g. GitHub). See the Nature Research guidelines for submitting code & software for further information.

Data

Policy information about availability of data

All manuscripts must include a data availability statement. This statement should provide the following information, where applicable:

- Accession codes, unique identifiers, or web links for publicly available datasets
- A list of figures that have associated raw data
- A description of any restrictions on data availability

The previously published ChIP-seq data that were reanalyzed here are available in the Gene Expression Omnibus (GEO) under accession codes GSE120060, GSE69566, GSE124225 and GSE123284. Previously published RNA sequencing data that were reanalyzed here are available under accession codes GSE106665 and GSE124227. Previously published ATAC-seq data that were reanalyzed here are available under accession codes GSE124224, GSE106665 and GSE101966. Metabolomics data have been deposited into MassIVE under accession code MSV000086347. Cancer cell line encyclopedia RNA sequencing data were downloaded from https://portals.broadinstitute.org/ccle/data/. The human lung adenocarcinoma, renal clear cell carcinoma, skin cutaneous melanoma and uterine corpus endometrial carcinoma data were derived from https://www.cbioportal.org/. Source data for unprocessed immunoblots for Fig. 1c, 2b, 2e-j, 3a, 3f and Extended

Data Fig. 1a-b, 2f, 2h, 3f and source data used for statistical analyses have been provided Source Data files. All other data supporting the findings of this study are available from the corresponding author on reasonable request.

Field-specific reporting

Please select the one below that is the best fit for your research. If you are not sure, read the appropriate sections before making your selection.

☒ Life sciences ☐ Behavioural & social sciences ☐ Ecological, evolutionary & environmental sciences

For a reference copy of the document with all sections, see nature.com/documents/nr-reporting-summary-flat.pdf

Life sciences study design

All studies must disclose on these points even when the disclosure is negative.

Sample size	No statistical method was used to predetermine sample size. Sample size was determined based on previous studies which has shown robust statistical power. Experiments were repeated 3 times experimentally unless otherwise stated for in vitro studies. At least 5 mice in each experimental groups were used for in vivo experiments.
Data exclusions	No data were excluded from the analyses.
Replication	At least two biologically independent replicates with similar results were performed.
Randomization	Experiments were all randomized.
Blinding	Investigators were blinded during data collection and analysis.

Reporting for specific materials, systems and methods

We require information from authors about some types of materials, experimental systems and methods used in many studies. Here, indicate whether each material, system or method listed is relevant to your study. If you are not sure if a list item applies to your research, read the appropriate section before selecting a response.

Materials & experimental systems

n/a	Involved in the study
☐	☒ Antibodies
☐	☒ Eukaryotic cell lines
☒	☐ Palaeontology
☐	☒ Animals and other organisms
☐	☒ Human research participants
☒	☐ Clinical data

Methods

n/a	Involved in the study
☒	☐ ChIP-seq
☐	☒ Flow cytometry
☒	☐ MRI-based neuroimaging

Antibodies

Antibodies used	Antibodies to the following proteins were used in the western blots: rabbit anti-ARID1A (Cell Signaling, cat. no. 12354, 1:1000 for western blot), rabbit anti-ARID1B (Abgent, cat. no. AT1190a, 1:1000 for western blot), rabbit anti-SMARCA4 (Cell Signaling, cat. no. 49360, 1:1000 for western blot) rabbit anti-GLS (Abcam, cat. no. 93434, 1:2000 for western blot), rabbit anti-SNF5 (Bethyl, cat. no. A301-087A, 1:1000 for western blot), rabbit anti-α-tubulin (Cell Signaling, cat. no. 2125, 1:2000 for western blot), mouse anti-?-actin (Sigma, cat. no. A5316, 1:5000 for western blot). hamster anti-CD3e (BD, cat. no. 552774, 1:1000 for flow cytometry), rat anti-CD45 (Biolegend, cat. no. 103147, 1:1000 for flow cytometry), rat anti-CD4 (Biolegend, cat. no. 100516, 1:1000 for flow cytometry), rat anti-CD8a (Biolegend, cat. no. 100708, 1:1000 for flow cytometry), hamster anti-CD69 (Biolegend, cat. no. 104510, 1:1000 for flow cytometry), rat anti-PD1 (Biolegend, cat. no. 109109, 1:1000 for flow cytometry) and rat anti-PDL1 (Biolegend, cat. no. 124321, 1:1000 for flow cytometry). The following antibodies were used for ChIP: rabbit anti-SNF5 (Bethyl, cat. no. A301-087A, 5 ug/IP), rabbit anti-BAF155 (Abcam, cat. no. ab172638, 2 ug/IP) and mouse anti-Pol II (Santa Cruz, cat. no. sc-47701, 5 ug/IP). Rabbit anti-ARID1A antibody (Abcam, cat.no. ab182560, 1:100 dilution) was used in the cut-and-run analysis.
Validation	Information of each antibody is available on the manufacturer's website. All the antibodies were validated by the manufacturers or in the published literatures. Several antibodies including rabbit anti-ARID1A, rabbit anti-ARID1B, rabbit anti-SMARCA4 and rabbit anti-GLS antibodies used in this manuscript for WB analysis have accompanying knockdown or knockout data. Rabbit anti-α-tubulin (Cell Signaling, cat. no. 2125) was validated by the manufacturer in C6, COS-7, NIH/3T3 and HeLa cells. Mouse anti-β-actin (Sigma, cat. no. A5316) was validated by the manufacturer in HeLa cells.

For the antibodies for flow cytometry:
hamster anti-CD3e (BD, cat. no. 552774) was validated by the manufacturer in splenocytes and thymocytes of BALB/c mice.
rat anti-CD45 (Biolegend, cat. no. 103147) was validated by the manufacturer in C57BL/6 mouse splenocytes.
rat anti-CD4 (Biolegend, cat. no. 100516) was validated by the manufacturer in C57BL/6 mouse splenocytes.
rat anti-CD8a (Biolegend, cat. no. 100708) was validated by the manufacturer in C57BL/6 mouse splenocytes.
hamster anti-CD69 (Biolegend, cat. no. 104510) was validated by the manufacturer in C57BL/6 mouse splenocytes.
rat anti-PD1 (Biolegend, cat. no. 109109) was validated by the manufacturer in splenocytes of BALB/c mice.
and rat anti-PDL1 (Biolegend, cat. no. 124321) was validated by the manufacturer in C57BL/6 mouse splenocytes.

For antibodies used for ChIP:
rabbit anti-SNF5 (Bethyl, cat. no. A301-087A) was validated by the manufacturer in HeLa cells.
rabbit anti-BAF155 (Abcam, cat. no. ab172638) was validated by the manufacturer in HEK293, HeLa, Jurkat and MDA-MB-231 cells.
mouse anti-Pol II (Santa Cruz, cat. no. sc-47701) was validated by the manufacturer in A-431, 3T3-L1, A-673, U-2 OS, HeLa and Jurkat cells.
rabbit Anti-ARID1A antibody (Abcam, cat.no. ab182560) was validated by the manufacturer in ARID1A wild-type HAP1 cells and ARID1A knockout HAP1 cells.

Eukaryotic cell lines

Policy information about cell lines

Cell line source(s)	Ovarian clear cell carcinoma cell lines (TOV21G, OVTOKO, OVISE, OVMANA and RMG1) were purchased from JCRB. Ovarian clear cell carcinoma cell line JHOC5 and JHOC7 and JHOC9 were purchased from Riken cell bank, and IGROV1 cells were obtained from NCI cell bank. Ovarian clear cell carcinoma cell line OVCA429 cells were obtained from MD Anderson Cell Lines Project. Rhabdoid tumor cell line G401, HEK293FT and Phoenix cells were purchased from ATCC. Renal clear cell carcinoma cell lines RCC4 and UMRC2 were obtained European Collection of Authenticated Cell Cultures (ECACC).
Authentication	All the cell lines are authenticated using short tandem repeat DNA profiling.
Mycoplasma contamination	Mycoplasma testing was performed using LookOut Mycoplasma PCR detection (Sigma) every month. Only Mycoplasma negative cells are used for the experiments.
Commonly misidentified lines (See ICLAC register)	No cell lines used in this study were found in the database of commonly misidentified cell lines that is maintained by ICLAC and NCBI Biosample.

Animals and other organisms

Policy information about studies involving animals; ARRIVE guidelines recommended for reporting animal research

Laboratory animals	Mice are maintained at 22-23 °C with 40-60% humidity and 12 hours light/12 hours dark cycle. For xenograft models, 6-8 weeks old female NSG mice; and For Arid1a-/-/Pik3caH1047R genetic ovarian clear cell ovarian carcinoma mouse model with C57BL/6J background, intrabursal adenovirus-Cre injection was used to induce ovarian clear cell carcinoma formation in 6-8 weeks old female mice.
Wild animals	No wild animals were used in this study.
Field-collected samples	No field-collected samples were used in this study.
Ethics oversight	The protocols were approved by the Institutional Animal Care and Use Committee (IACUC) of the Wistar Institute.

Note that full information on the approval of the study protocol must also be provided in the manuscript.

Human research participants

Policy information about studies involving human research participants

Population characteristics	*Describe the covariate-relevant population characteristics of the human research participants (e.g. age, gender, genotypic information, past and current diagnosis and treatment categories). If you filled out the behavioural & social sciences study design questions and have nothing to add here, write "See above."*
Recruitment	*Describe how participants were recruited. Outline any potential self-selection bias or other biases that may be present and how these are likely to impact results.*
Ethics oversight	The protocol for using primary cultures of human ovarian clear cell tumor cells was approved by the University of British Columbia Institutional Review Board (H18-01652). Informed consent was obtained from human subjects. All relevant ethical regulations have been complied with.

Note that full information on the approval of the study protocol must also be provided in the manuscript.

Flow Cytometry

Plots

Confirm that:

☒ The axis labels state the marker and fluorochrome used (e.g. CD4-FITC).

☒ The axis scales are clearly visible. Include numbers along axes only for bottom left plot of group (a 'group' is an analysis of identical markers).

☒ All plots are contour plots with outliers or pseudocolor plots.

☒ A numerical value for number of cells or percentage (with statistics) is provided.

Methodology

Sample preparation	For immune cell profiling, tumor cells were extracted using Mouse Dissociation Kit. The cells were then mashed with 70-µM strainer and used for staining. For peritoneal wash, peritoneal cavity of mice was washed three times with 5 ml PBS and incubated in RBC lysis buffer. Live/dead cells were discriminated by Zombie Yellow™ Fixable Viability Kit.
Instrument	LSRII-14 flow cytometer and LSRII-18 flow cytometer
Software	Data were acquired using BD FACSDiva Version 8.0 and analyzed using FlowJo v10.0.7 software
Cell population abundance	10000 cells were used to sort and at approximately 90% cells were used to analyze.
Gating strategy	Cell debris were removed using FSC-A and SSC-A. Doublets were removed from total population using FSC-A and FSC-H. Live cells were gated by Live/Dead AmCyan-A. Single staining were used for compensation calculation. Positive population were gated based on comparing unstained samples and single stained sample as described in the Extended Data Fig.6a.

☒ Tick this box to confirm that a figure exemplifying the gating strategy is provided in the Supplementary Information.